https://doi.org/10.5194/acp-2022-193
Preprint. Discussion started: 25 April 2022

Atmospheric Chemistry and Physics Discussions

Derivation and validation of top-down African biomass burning CO emissions and fuel consumption measures derived using geostationary FRP data and Sentinal-5P TROPOMI CO retrievals

Hannah M. Nguyen[1,2], Jiangping He[1,3], Martin J. Wooster[1,2,3]

[1]Department of Geography, King's College London, London, WC2R 2ND, UK
[2]Leverhulme Centre for Wildfires, Environment and Society, UK
[3]National Centre for Earth Observation (NCEO), UK

Correspondence to: Hannah M. Nguyen (hannah.nguyen@kcl.ac.uk)

Abstract: We present the first top-down CO fire emissions inventory for Africa based on the direct relation between geostationary satellite-based Fire Radiative Power (FRP) measures and satellite observations of Total Column Carbon Monoxide (TCCO). This work extends significantly the previous Fire Radiative Energy Emissions (FREM) approach that derived Total Particulate Matter (TPM) emission coefficients from FRP measures and Aerosol Optical Depth (AOD) observations. The use of satellite-based CO observations to derive CO emission coefficients, C_e^{CO}, addresses key uncertainties in the use of AOD measures to estimate fire-generated CO emissions including; the requirement for a smoke mass extinction coefficient in the AOD to TPM conversion; and the large variation in TPM emission factors - which are used to convert TPM emissions to CO emissions. We use the FREM-derived CO emission coefficients to produce a Pan-African CO fire emission inventory spanning 16 years. Regional CO emissions are in close agreement with the most recent version of GFED(v4.1s), despite the two inventories using completely different satellite datasets and methodologies to derive CO emissions. Dry Matter Consumed (DMC) and DMC per unit area values are generated from our CO emission inventory – the latter using the 20 m resolution Sentinal-2 FireCCISFD burnt area (BA) product for 2019. We carry out an evaluation of our FREM-based CO emissions by using them as input in the WRF-CMAQ chemical transport model and comparing simulated TCCO fields to independent Sentinal-5P TROPOMI TCCO observations. The results of this validation show FREM CO emissions to generally be in good agreement with these independent measures - particularly in the case of individual fire-generated CO plumes where modelled in-plume CO was within 5% of satellite observations with a coefficient of determination of 0.80. Modelled and observed CO, averaged over the full model domain, are within 4% of each other, though localised regions show an overestimation of modelled CO by up to 50%. However, when compared to other evaluations of current state-of-the-art fire emissions inventories, the FREM CO emission inventory derived in this work shows some of the best agreement with independent measures. Updates to the previously published FREM TPM emissions coefficients are also provided in the Appendix of this article, along with a satellite and ground-based validation of this FREM TPM emissions inventory. The methodology and resulting CO fire inventory described in this work will form the basis of an upcoming operational LSASAF CO fire emissions product for Africa.

https://doi.org/10.5194/acp-2022-193
Preprint. Discussion started: 25 April 2022

Atmospheric Chemistry and Physics Discussions

1 Introduction

The open burning of biomass in landscape fires is amongst the largest contributor of gaseous and particulate emissions to the atmosphere. In many regions such fires show significant interannual variability, and together global biomass burning generates a significant fraction of many atmospheric species, including for example the pollutants total particulate matter (TPM) and carbon monoxide (CO) (Andreae and Merlet, 2001; Bowman et al., 2009; Forster et al., 2007). Landscape fire emission inventories are thus essential to many studies in Earth system science (Keywood et al., 2013; Langmann et al., 2009), and also to "real-time" decision-making applications such as air quality forecasting. Fire emissions inventories are often constructed using a 'bottom-up' approach in which estimates of dry matter consumed (DMC) are estimated from satellite-derived metrics of burned area (BA), or occasionally active fire counts, combined with information on pre-fire fuel load and combustion completeness (Seiler and Crutzen, 1980). The resulting DMC estimates are then multiplied by biome-specific emission factors (EFs) that relate each kilogram of burned biomass to the amount of a trace gas or aerosol species released. EFs are typically derived from small scale laboratory or ground-based field measurements (Akagi et al., 2011; Andreae, 2019; Andreae and Merlet, 2001), along with airborne sampling of fire plumes (Abel et al., 2003; Lavorel et al., 2007; Quennehen et al., 2012). The Global Fire Emissions Database (GFED) is the most widely-used 'bottom-up' fire emissions inventory (van der Werf et al., 2006, 2010, 2017), but the reliance on burned area and pre-fire fuel load information means it cannot provide near real-time information. The Global Fire Assimilation System (GFAS) (Kaiser et al., 2012) uses near-real time satellite observations of actively burning fires (AFs) to drive its DMC estimates, performing the conversion using a previously-derived calibration relationship that relates a biome's fire radiative energy (FRE) to DMC totals coming from GFED. The primary advantage over GFED is the near real-time aspect, capable of delivering information suitable for driving atmospheric models in forecast mode. The main disadvantage is the fact that the relatively uncertain fuel load and combustion completeness assumptions, which introduce some of the most significant uncertainty to burned-area based fire emissions calculations, are incorporated into GFAS via this calibration (Kaiser et al., 2012; Reid et al., 2009; Zhang et al., 2008). Other global fire emissions inventories such as FLAMBE (Reid et al., 2009) and FINN (Wiedinmyer et al., 2011) contain aspects of the same methodologies and thus suffer similar uncertainty sources.

Recently so-called fully 'top-down' fire emissions methodologies have evolved, partly in an attempt to remove the limitations induced by calibrating satellite-derived FRE measures against DMC totals produced by e.g. GFED. These 'top-down' methodologies include the Fire Energetics and Emissions Research (FEER) approach of Ichoku and Ellison (2014) and FREM (Mota and Wooster, 2018; Nguyen and Wooster, 2020). The FEER and FREM approaches derive landscape fire emissions estimates directly from EO-derived FRE measures, removing the step requiring calculation of DMC and thus the uncertainties inherent in that calculation. In each method, a scalar (a so-called "smoke emission coefficient"; C_e^x in g.MJ^{-1}) is generated for each fire-affected biome to capture the relationship between the rate of FRE emission (i.e. the so-called fire radiative power [FRP] of the causal fire) and the associated emission rate of a particular trace gas or aerosol species, x. Importantly, because

https://doi.org/10.5194/acp-2022-193
Preprint. Discussion started: 25 April 2022


Atmospheric Chemistry and Physics Discussions

C_e^x values derived from laboratory fire measurements (e.g. as per Freeborn et al., 2008) may not be fully representative of all the effects relevant to satellite data of real landscape fires (Freeborn et al., 2008; Mota and Wooster, 2018), the FEER and FREM approaches instead used C_e^x values derived from the satellite datasets themselves. Specifically, individual fire matchups where the fires' radiative energy emissions and its smoke plume observed from satellite are used to generate the C_e^x values. Thus far, both FEER and the FREM approaches have focused on smoke plume observations of aerosol optical depth (AOD), which are used to create in-plume values of total particulate matter (TPM) via application of a smoke aerosol mass extinction coefficient, β_e (in $m^2.g^{-1}$) (as described Ichoku and Ellison (2014) and Nguyen and Wooster (2020)). Once representative C_e^{TPM} values are obtained using this matchup dataset, they can be applied to the FRP data of any fire to derive its rate of TPM emission – including from near real-time satellite data feeds. The FEER approach of Ichoku and Ellison (2014) uses polar orbiting MODIS data to provide the FRP records driving its TPM emissions estimates, whilst FREM uses the far higher-temporal-resolution FRP data available from geostationary satellites. The latter provides the highest temporal frequency TPM emissions estimates currently available (Nguyen and Wooster, 2020), and this type of high frequency emission information has been shown useful for maximising the accuracy of smoke transport modelling (Baldassarre et al., 2015; Garcia-menendez et al., 2014). The use of geostationary FRP data with FREM also allows a simple temporal integration to be used to calculate FRE (see Nguyen and Wooster (2020)), obviating the need for assumptions about the plume height, wind speed and wind direction used by FEER when deriving C_e^{TPM} from individual MODIS FRP measures (Ichoku and Ellison, 2014). The purpose of the current work is to adapt the FREM approach further to derive trace gas emissions estimates directly from the FRP observations, without first estimating TPM emissions as a precursor. The Mota and Wooster (2018) and Nguyen and Wooster (2020) iterations of FREM both estimated emissions of trace gas x (e.g. carbon monoxide) via an emissions coefficient [C_e^{CO}] derived from Equation 1 and the emission coefficient of a 'reference' species (thus far always TPM):

$$C_e^x\ [g.MJ^{-1}] = \frac{EF_x\ [g.kg^{-1}]}{EF_{reference}\ [g.kg^{-1}]} \cdot C_e^{reference}\ [g.MJ^{-1}] \qquad [1]$$

Where C_e^x is the biome-specific emission coefficient for trace gas species x (e.g. CO), EF_x is the species x emission factor for that biome, $EF_{reference}$ is the emission factor for the reference species in that biome, and $C_e^{reference}$ is the FREM-based smoke emission coefficient for the references species in that biome.

Use of Equation 1 to generate trace gas emissions coefficients does introduce some uncertainty, mainly due to the emissions factors of the reference species used thus far [TPM] typically being far from constant even in a single biome - EF_{TPM} is relatively poorly constrained in tropical forest and cultivated land for example (Akagi et al., 2011; Andreae, 2019). Here we aim to directly generate [C_e^{CO}] emission coefficients by replacing the matchup fire plume AOD information currently used by FREM (Nguyen and Wooster, 2020) with that of total column CO (TCCO) derived from Sentinel-5P TROPOMI observations (Landgraf et al., 2016). CO concentrations in landscape fire plumes are far higher than in the ambient atmosphere (e.g. Wooster

https://doi.org/10.5194/acp-2022-193
Preprint. Discussion started: 25 April 2022


Atmospheric Chemistry and Physics Discussions

et al., 2011), thus providing potential for distinct contrasts between a smoke plume and its background in the TROPOMI TCCO record. A further advantage of generating C_e^{CO} values directly and not via Equation 1 is that the smoke aerosol mass extinction coefficient (β_e) used to generate TPM estimates from AOD measures is itself somewhat dependent on fuel type burned, smoke aging and atmospheric relative humidity (Chin et al., 2002; Formenti et al., 2003; Reid et al., 2005). Direct use of satellite TCCO retrievals to derive C_e^{CO} removes this uncertainty source from FREM-derived estimates of trace gas emissions coming from the satellite FRP retrievals.

2 Methodology

2.1 FRP and CO Datasets

Africa is the most fire affected continent on the planet (van der Werf et al., 2017), and to derive C_e^{CO} we focused on matchup fires observed across Africa's fire-affected biomes by the geostationary Meteosat SEVIRI instrument and by the polar-orbiting Sentinel-5P TROPOMI sensor. The Meteosat FRP-PIXEL product is generated every 15-minutes from SEVIRI observations and issued in near real-time by the EUMETSAT LSA SAF (https://landsaf.ipma.pt/en/data/catalogue/), whilst daily 7 km spatial resolution TROPOMI total column carbon monoxide (TCCO) data can be downloaded from Sentinel-5P Pre-Operations Data Hub (https://scihub.copernicus.eu/).

Under cloud-free conditions, which predominate during African fire seasons, the FRP-PIXEL product provides almost continuous landscape fire observations. The coarser pixel size of geostationary observations mean they have a higher minimum FRP detection limit than do polar-orbiting FRP datasets such as those from MODIS and VIIRS (Roberts et al., 2005, 2015). However, the AFs detectable in the geostationary FRP products still remain significantly smaller in terms of pixel area coverage (e.g. down to perhaps 0.01% of the pixel) than the minimum burned area detectable in the MODIS burned area products - which are the most common data source of 'bottom-up' fire emission estimation approaches (Van Leeuwen et al., 2014; Reid et al., 2009; Vermote et al., 2009). Furthermore, a recent comparison between AFs detected by the 30 m spatial resolution Landsat-8 Operational Land Imager (OLI) and Meteosat FRP-PIXEL data showed the geostationary product to have an 8% error of commission, 'false alarm rate' (Hall et al., 2019), very similar to that of the widely used MODIS AF products (Giglio et al., 2016). Prior comparisons between the SEVIRI FRP-PIXEL AF product and 1 km MODIS AF data have identified the FRP-PIXEL products AF error of omission rate and rate of FRP underestimation compared to MODIS (Roberts et al., 2015; Wooster et al., 2015), and following Mota and Wooster (2018) we apply this spatially varying 'small fire adjustment' factor to account for fires burning below the SEVIRI sensor's minimum FRP detection limit. We also apply the cloud cover correction used in the LSA SAF Meteosat FRP-GRID product detailed in (Wooster et al., 2015), though the sparse cloud cover of the African fire season significantly limits the effect of this adjustment. To aid identification of suitable fire matchups we also use visual band data from the Visible/Infra-red Imager and Radiometer Suite (VIIRS) onboard the Suomi-NPP (National Polar-

https://doi.org/10.5194/acp-2022-193
Preprint. Discussion started: 25 April 2022

Atmospheric Chemistry and Physics Discussions

orbiting Partnership) satellite. Suomi-NPP overpasses within 3.5 minutes of the Sentinel-5P overpass and provides 375 m and 750 m spatial resolution imagery that greatly benefits plume identification in the TROPOMI CO data. VIIRS imagery data were obtained from https://ladsweb.modaps.eosdis.nasa.gov/.

2.2 Top-down FREM-CO Methodology

As introduced in Section 1, the FREM methodology derives a biome-dependent 'smoke emission coefficient' for a reference species y, $[C_e^y]$ from the relationship between the thermal energy a fire radiates (i.e. the FRE in MJ) and the mass of the target compound y it emits (in kg or g). Focusing on CO, we derived $[C_e^{CO}]$ from a set of matchup fires for which good observations of both FRE and TCCO in the plume exist. The derived C_e^{CO} has units of g.MJ^{-1} or g.s^{-1}.MW^{-1} and can then be used to generate rates or totals of CO emissions when applied to further FRP or FRE data respectively. Sentinel-5P CO retrievals are available from May 2018 until the present day, and we gathered our matchup data from joint Sentinel-5P TCCO, Meteosat FRP-PIXEL, and VIIRS imagery data covering July to December 2018 and the full year of 2020. For each fire we calculate (i) total smoke plume CO [g] from the TROPOMI TCCO retrievals, and (ii) total FRE [MJ] released for the period the plume was generated over from FRP-PIXEL data of the fire - integrated from the time of the first AF detection to the moment of the Sentinel-5P overpass.

We studied both Northern and Southern Hemisphere Africa (NHAF and SHAF), which have temporally different fire seasons. We derived C_e^{CO} for each of the fire biomes defined in NHAF and SHAF by Nguyen and Wooster (2020), which are themselves based on re-classification of a 2019 landcover map generated from 300 m spatial resolution MERIS and PROBA-V observations as part of the European Space Agency (ESA) Climate Change Initiative (CCI) (https://cds.climate.copernicus.eu/cdsapp#!/dataset/satellite-land-cover). To provide further biome discrimination for *woodland savanna/open forest*, we made use of percentage tree cover information (above 5 m height), taken from a 2015 map of Vegetation Continuous Fields (VCF) generated from 30 m Landsat data (https://landsat.gsfc.nasa.gov/). In total six fire biomes were defined for which individual C_e^{CO} were generated - *closed canopy forest*, *low-woodland savanna/open forest*, *high-woodland savanna/open forest*, *grassland*, *shrubland* and *managed land*. Only fires for which a single biome represented more than 50% of the observed FRP pixels in a fire were considered for use as a potential matchup fire during C_e^{CO} derivation, and for each fire we inspected the FRP-PIXEL Quality Product detailed in (Wooster et al., 2015) to filter out any that were partly cloud-obscured prior to the Sentinel-5P overpass. The final set of matchup fires in each of the six biomes had their plume outlined, together with a buffer to represent the surrounding ambient atmosphere. Plume outlines were based on the Sentinel-5P TCCO product and the near co-incident VIIRS imagery (Figure 1). The minimum CO value within the buffer of each plume was used to calculate the ambient atmosphere 'background' CO concentration, from which the CO 'excess above

https://doi.org/10.5194/acp-2022-193
Preprint. Discussion started: 25 April 2022

Atmospheric Chemistry and Physics Discussions

background' in each TROPOMI pixel was calculated. Summing this excess over all plume pixels thus provided the total amount of fire-emitted CO in the plume for that matchup fire. This was then compared to the total amount of FRE released over the period from the start of the fire to when the plume observation was made, forming one datapoint on the relevant biome graph of **Figure 2**.

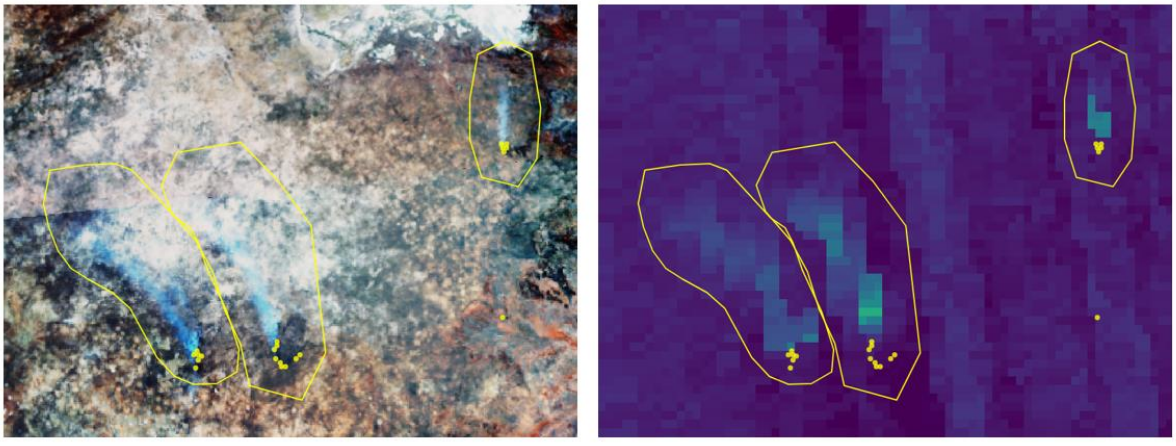

Figure 1. Example data of a matchup fires used to develop the C_e^{CO} smoke emissions coefficients presented in Figure 2. (a) VIIRS RGB image of three landscape fire smoke plumes, along with (b) the corresponding image of Sentinel-5P derived total column CO (TCCO). In both images, the AF pixel detections taken from the Meteosat FRP-PIXEL product are superimposed (yellow points) along with the bounding polygons used to delineate the fire plumes. Satellites data are from 11:24 and 11:30 UTC respectively, on September 9th over an area in norther Botswana.

2.3 Derivation of Carbon Monoxide Smoke Emission Coefficients [C_e^{CO}]

The set of matchups for each fire affected biome are shown in Figure 2 and were used to derive the set of biome-dependent CO smoke emission coefficients [C_e^{CO}] listed in Table 1 using zero-intercept ordinary least squares (OLS) regression. Nguyen and Wooster (2020) used instead orthogonal distance regression (ODR) for the derivation of their TPM emission coefficient values [C_e^{TPM}], so to ensure a consistent methodology for emission coefficient derivation we also re-derived C_e^{TPM} values using OLS regression from the Nguyen and Wooster (2020) dataset (see Appendix A). The updated C_e^{TPM} for closed canopy forest, managed land, grassland, shrubland, low-woodland savanna and high-woodland savanna are 26.07 g.MJ^{-1}, 12.23 g.MJ^{-1}, 9.39 g.MJ^{-1}, 9.88 g.MJ^{-1}, 10.65 g.MJ^{-1}, and 14.18 g.MJ^{-1} respectively, and on average these are 14% lower than the C_e^{TPM} reported in Nguyen and Wooster (2020) which were based on the same matchup data but derived via ODR regression. These updated C_e^{TPM} are the ones reported and used hereafter. The method used to evaluate our final CO emissions in Section 4 using the WRF-CMAQ model and regional atmospheric CO observations was also used to carry out an analogous evaluation of the TPM emissions generated from the updated C_e^{TPM} values of Appendix A – but replacing the CO observations with AERONET and MODIS MAIAC AOD data (see

https://doi.org/10.5194/acp-2022-193
Preprint. Discussion started: 25 April 2022


Atmospheric Chemistry and Physics Discussions

Appendix C).

For each of the six fire biomes at least 12 matchup fires were available for derivation of C_e^{CO}, apart from for closed canopy forest. TROPOMI CO plumes in the closed canopy forest biome were not sufficiently distinct from the background in this region, so we instead derived C_e^{CO} for closed canopy forest from a 'FEER-equivalent' value. The method used to derive this is detailed in Nguyen and Wooster (2020), and essentially involves aggregating the FEER C_e^{TPM} emission coefficients of Ichoku and Ellison (2014) (https://feer.gsfc.nasa.gov/data/emissions/) to the relevant fire biome. Equation 1 was then applied to obtain a FEER-equivalent C_e^{CO}, this was calculated as 156.7 g.MJ^{-1} for the closed canopy forest biome. We generated FEER-equivalent C_e^{CO} for each of the other five fire biomes to compare these to our directly derived C_e^{CO} values. We found agreement for all biomes was within ±34% (see Table 1), somewhat justifying our use of the FEER-equivalent value in the closed canopy forest biome where a directly derived C_e^{CO} value was not achieved.

For ease of future discussion, hereafter, we will refer to emissions inventories generated using the C_e^{CO} coefficients of this Section as the FREM_bCO emissions inventory. Any emissions inventory generated using the updated C_e^{TPM} coefficients reported in **Table 1** and detailed in Appendix A will be referred to as FREM_bTPM hereafter - the *b* in both cases denotes the *base* or reference species used to produce emissions estimates.

https://doi.org/10.5194/acp-2022-193
Preprint. Discussion started: 25 April 2022

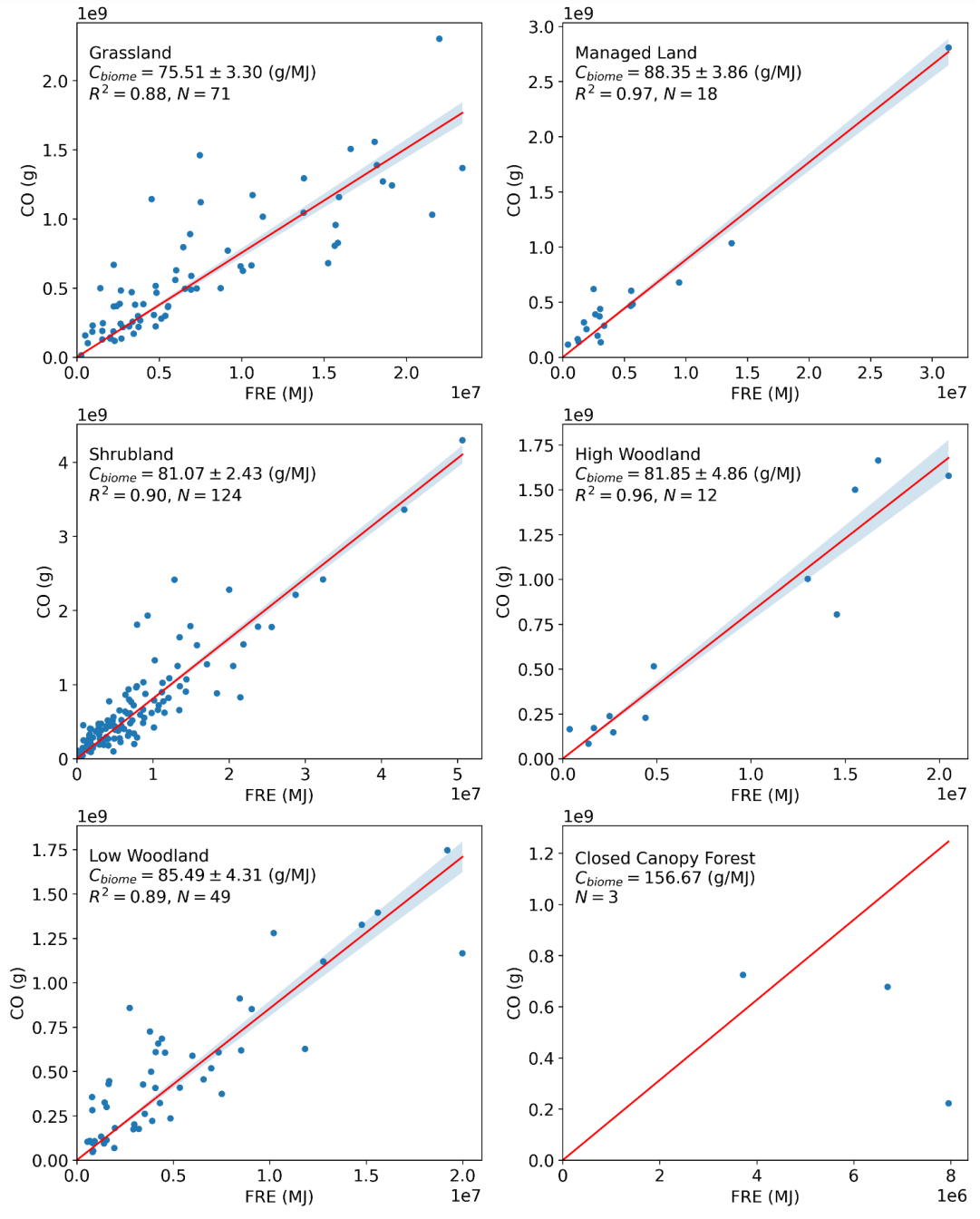

Figure 2. Carbon monoxide smoke emission coefficients (C_e^{CO}; in g.MJ-1) derived from matchup fires burning across the six fire-affected biomes shown mapped in Figure 8b across southern hemisphere Africa (note that the matchup fires here come from both African hemispheres). Each C_e^{CO} is derived from the slope of an ordinary least squares (OLS) regression between the fire-emitted CO calculated from Sentinel-5P total column CO (TCCO) observations and the fire's matching FRE. The shaded grey area indicates the error of each slope. Closed canopy forest had insufficient matchup fires identified and so C_e^{CO} for this biome was derived using the FEER-equivalent procedure detailed in Section 2.3 and in Nguyen and Wooster (2020). Datapoints from the three matchup fires that were identified in closed canopy forest are included in the plot.

https://doi.org/10.5194/acp-2022-193
Preprint. Discussion started: 25 April 2022

Atmospheric Chemistry and Physics Discussions

Table 1. Biome-dependent CO smoke emission coefficients (C_e^{CO} *in* $g.MJ^{-1}$) as derived from the data shown in Figure 1. Also shown are the matching values calculated using the updated FREM C_e^{TPM} values from Appendix A and FEER-equivalent coefficient values produced from the FEER product of Ichoku & Ellison (2014), aggregated to the FREM biomes (see Nguyen and Wooster (2020) for full details). *Figure 1 shows insufficient matchup fires were found for the closed canopy forest biome, so the FEER-equivalent value is reported instead and used hereafter.

Fire Affected Biome	Sentinal-5P TCCO-derived C_e^{CO} (Section 2.2)	C_e^{CO} calculated via updated FREM C_e^{TPM} (see Appendix A)	FEER-equivalent (see Nguyen & Wooster 2020)
Closed Canopy Forest	156.7*	248.7	156.7
Managed Land	88.4	72.1	100.7
Grassland	75.5	74.5	87.5
Shrubland	81.1	78.4	87.4
Low-woodland savanna	85.5	84.5	101.9
High-woodland savanna	81.9	112.5	110.1

3 FREM Fire Emission Inventory

3.1 CO Emissions

Following derivation of C_e^{CO} for each of the six fire biomes of NHAF and SHAF (Table 1), a set of landscape fire emission rates and totals for these regions were derived via application of C_e^{CO} to the complete Meteosat FRP-PIXEL data record of 2004 to 2019 (Wooster et al., 2015). To account for possible changes in landcover, fire biome maps for 2005, 2010 and 2015 were produced in an analogous method to that used to generate the 2019 map (i.e., based on the CCI Landcover and Landsat VCF data products of these years). The Meteosat FRP-PIXEL record was combined with this set of biome maps and the C_e^{CO} values of Table 1 to produce a 16 year record of African fire emissions. This FREMs_bCO inventory is the highest spatio-temporal resolution fire emissions inventory for CO yet available over Africa (15 min, 3 km at the sub-satellite point), and monthly totals with the cloud and small fire correction applied are shown in Figure 3 alongside those of the most current version of the Global Fire Emissions Database (GFEDv4.1s; van der Werf et al., 2017; www.globalfiredata.org/). GFED4.1s includes its own 'small fire' correction to account for burns un-detected in the 500 m MODIS MCD64A1 burned area product. Mean annual CO emission totals are detailed for both inventories with and without their respective small fire corrections applied in Table 2.

https://doi.org/10.5194/acp-2022-193
Preprint. Discussion started: 25 April 2022

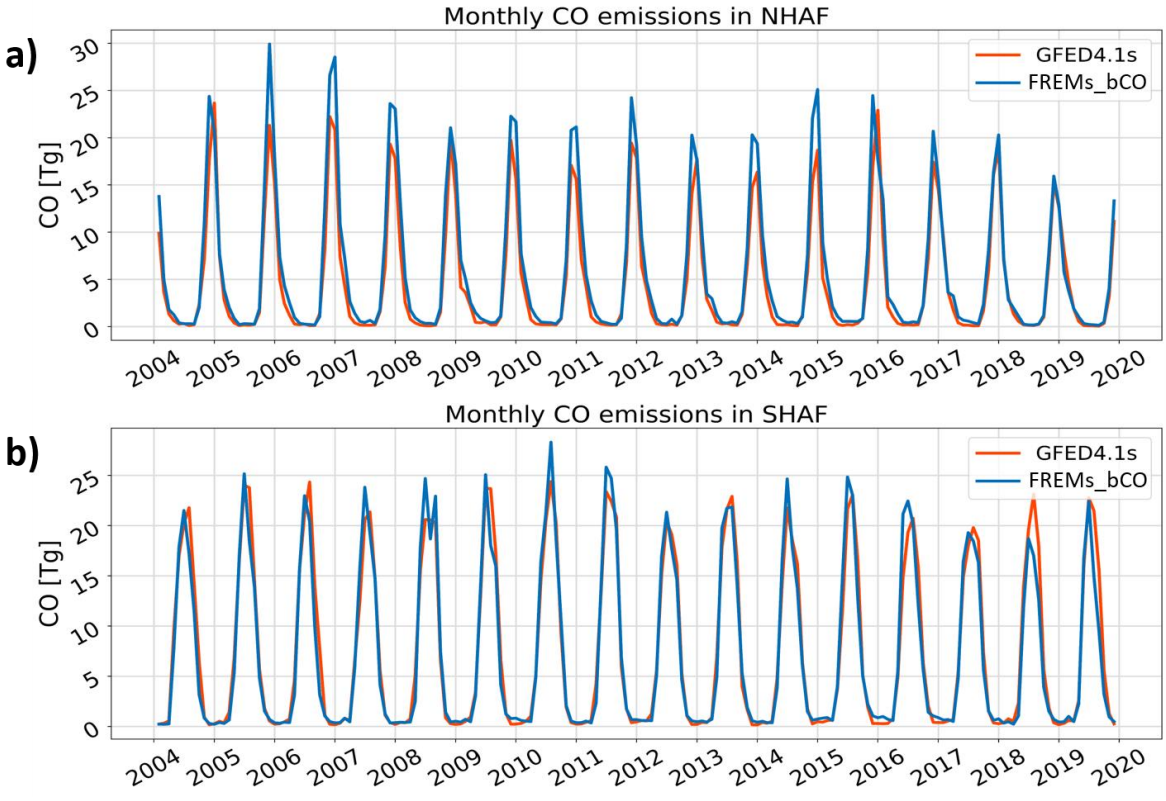

Figure 3. Monthly landscape fire CO emissions over a 16-year period for (a) northern and (b) southern hemisphere Africa, as derived in FREMs_bCO and GFED4.1s, both with their respective 'small fire correction' applied ("s" indicates its application)

https://doi.org/10.5194/acp-2022-193
Preprint. Discussion started: 25 April 2022

Atmospheric Chemistry and Physics Discussions

Table 2. Mean annual CO fire emission totals for the period 2004 to 2019 as derived for northern and southern hemisphere Africa using the FREM methodology developed herein and reported alongside those of GFEDv4.1. Values are reported as those both with and without the relevant 'small fire correction' applied ("s" indicates its application), as well as the % difference made by this upward adjustment.

		NHAF Total CO Emissions [Tg]	SHAF Total CO Emissions [Tg]
Without small fire correction applied	FREM_bCO	46.6	64.4
	GFED4.1	40.5	67.5
With small fire correction applied	FREMs_bCO	70.1	87.2
	GFED4.1s	55.9	90.2
FREM_bCO	% effect of small fire correction	50.4	35.4
GFED4.1	% effect of small fire correction	38.0	36.7

The FREMs_bCO and GFEDv4.1s CO emissions time-series shown in Figure 3 show very similar magnitudes, particularly in SHAF. Table 2 confirms that the mean annual totals are also close, with FREMs_bCO 25% higher than that of GFED4.1s in NHAF, and 3% lower in SHAF. The small fire (SF) corrections of both inventories also increase the basic CO emissions calculated in each inventory by similar a magnitude, especially in SHAF. The closeness of these results is noteworthy when considering that these CO emissions estimates have been produced using completely different methodologies and with no input data, conversion variables or emissions factors in common. Figure 3 also shows similar temporal patterns for monthly CO emissions between the two inventories, with annual peaks and minima generally occurring in the same years. However, as Mota and Wooster (2018) and Nguyen and Wooster (2020) noted for TPM emissions, the FREM methodology often predicts a slightly earlier emissions peak in SHAF compared to GFED. This shift agrees with the fact that FRP measures seem to peak in SHAF a month or so earlier than do BA measures (e.g. (Zheng et al., 2018) who compare GFED BA with GFAS FRP). However, the same work also suggests that CO emissions may actually lag BA by a month in SHAF based on MOPITT CO observations, as does the work of and Ito et al. (2008), adding complexity to the interpretation.

A more spatially detailed intercomparison is shown in Figure 4, which examines a month of FREMs_bCO hourly average CO emissions in two of the most fire affected countries in Africa - the Central African Republic (CAR) and Angola during January and August 2012 respectively (typically their peak fire months). Our mean hourly CO emissions for CAR in January are lower than those of GFED4.1s by 40%, whereas for Angola in August they are 60% higher. The very strong fire emissions diurnal

https://doi.org/10.5194/acp-2022-193
Preprint. Discussion started: 25 April 2022

Atmospheric Chemistry and Physics Discussions

cycle is highly resolved by the FREM inventory, demonstrating the data richness provided by the high temporal resolution of the geostationary FRP observations used. An additional benefit is that, unlike burned area data, FRP measures from geostationary satellites are available in near real time and thus the FREM emissions of CO, TPM and other air pollutants are potential sources of data for air quality forecasting (Roberts et al., 2015).

The small differences seen between the FREMs_bCO and GFEDv4.1s CO emissions at the hemisphere scale (Figure 3) compared to the larger country-level differences (Figure 4) demonstrate how emissions inventories may be similar in magnitude at larger scales, but can vary significantly more at the local scale. Zhang et al. (2014) compared modelled AOD fields generated from seven commonly used fire emissions inventories using an atmospheric transport model and demonstrated that the maximum variation between the modelled AOD averages of these inventories increased significantly when moving from regional to local scale in Northern Sub-Saharan Africa.

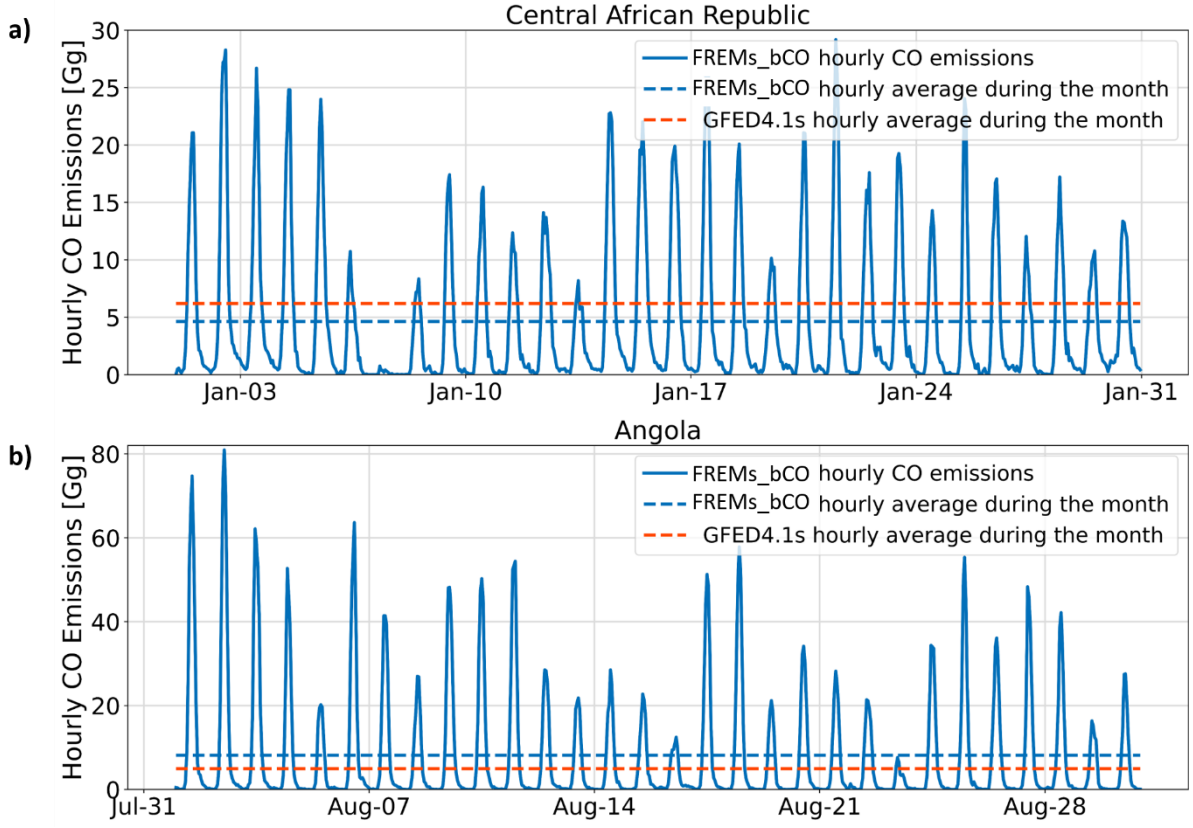

Figure 4. Hourly FREMs_bCO emissions from landscape fires burning over a month-long period in 2012 during the peak fire season of (a) Central African Republic and (b) Angola. The monthly mean of this emission rate is also shown, along with that from GFEDv4.1s.

https://doi.org/10.5194/acp-2022-193
Preprint. Discussion started: 25 April 2022


Atmospheric Chemistry and Physics Discussions

Past comparisons made between modelled CO atmospheric concentrations driven by GFED, and CO observations coming from instruments such as MOPITT (Worden et al., 2010) suggest that GFEDv3 underestimated African CO emissions by up to 50% (Chevallier et al., 2009; Kopacz et al., 2010; Pechony et al., 2013). Since GFEDv3 and GFEDv4.1s CO emissions are similar both for NHAF and SHAF, this points to a possible continued underestimation of CO emissions by GFEDv4.1s over Africa. Each GFED version uses the 500 m MODIS MCD64A1 burned area product as their driving data, and recent studies have shown African burned area to be far higher than MODIS estimates when mapped using 20 m Sentinel-2 MSI or 30 m Landsat imagery (Hawbaker et al., 2017; Roteta et al., 2019; Tsela et al., 2010). This underestimation by the MODIS BA product is the theoretical basis for requiring the 'small fire correction' in GFEDv4.1 (Randerson et al., 2012; van der Werf et al., 2017). However, the relatively good agreement seen between GFEDv4.1s and the FREMs_bCO inventory compared herein (e.g. Figure 3) - which are developed from completely different datasets and approaches - suggests African CO emissions may not be so underestimated as past CO observations have suggested when small fires are accounted for. Reconciling top-down and bottom-up derived CO fire emission inventories with observations of CO made from low-earth orbit remains a continuing research focus.

3.2 Dry Matter Consumed

Unlike with bottom-up approaches, where DMC [kg] is calculated first and converted to species emissions estimates using estimates of fuel load, combustion completeness and species emissions factors (see Section 1), within the FREM approach fire emissions are estimated directly and DMC can then be calculated from these if required. In this case, DMC is estimated by dividing the emissions total by the species emissions factor, an approach first demonstrated by Mota and Wooster (2018) using TPM as the relevant species. CO is the second greatest emitted product from biomass burning, and the emissions factor of CO is far more consistent and well constrained than that of TPM (Akagi et al., 2011; Andreae, 2019). Therefore, the FREM-derived CO emissions detailed in Section 3 can be related to DMC far more confidently and more consistently than those of TPM. Monthly FREM-derived DMC emissions generated from this approach for CAR and Angola are shown in Figure 5 alongside those from GFED4.1s. The former are lower at the peak of the CAR fire season compared with those of GFEDv4.1s, but consistently higher at the Angolan fire season peak. Either side of these peaks there is very good agreement between the two.

https://doi.org/10.5194/acp-2022-193
Preprint. Discussion started: 25 April 2022

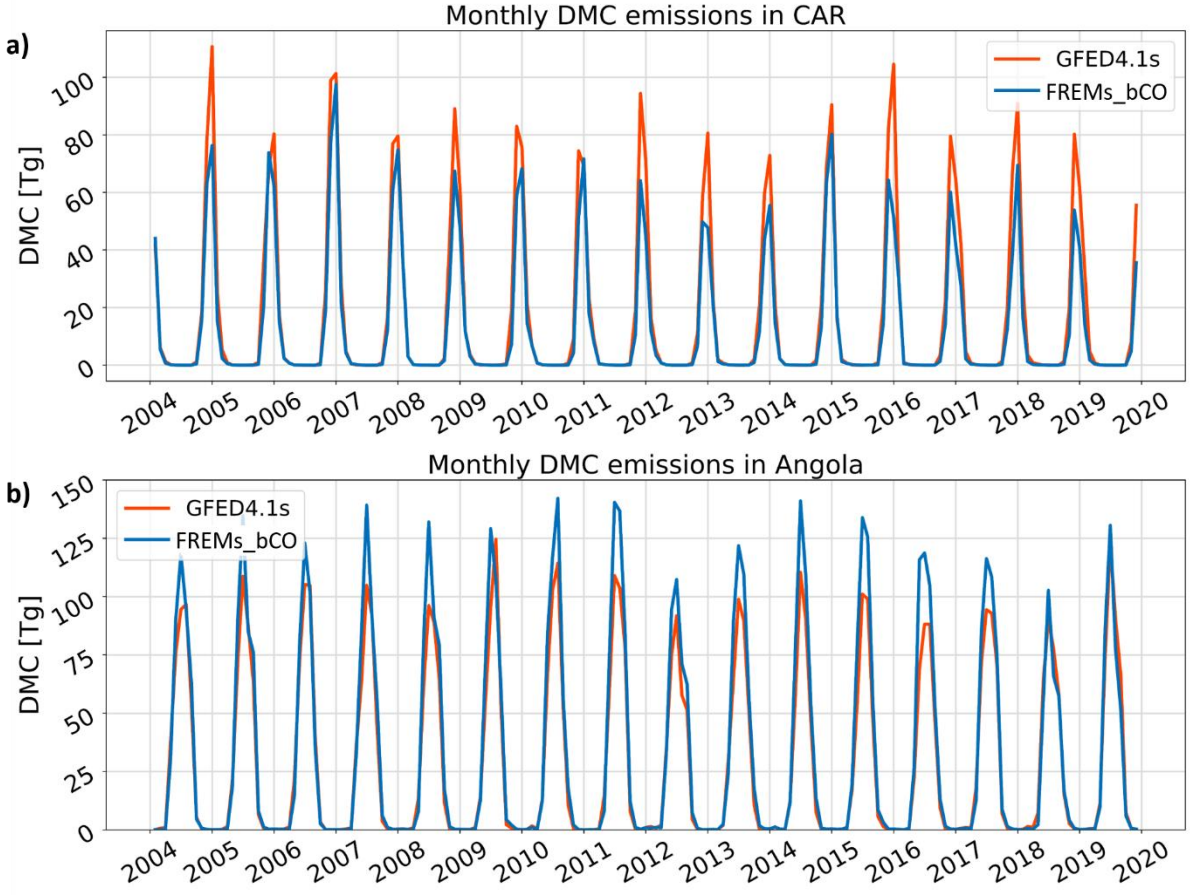

Figure 5 Monthly dry matter consumed (DMC in g) for a 16-year period as derived from FREMs_bCO CO emissions and that of GFED4.1s for (a) Central African Republic (CAF) and (b) Angola.

300

Once calculated, DMC can be further combined with burned area information to generate DMC per unit area measures across the African region – the only observational based approach capable of doing this at present (Nguyen and Wooster, 2020). We use FREM-derived DMC with the Sentinel-2 20 m spatial resolution FireCCI Small Fire Dataset (v2.0) for 2019 to calculate DMC per unit area at a 0.1° resolution in that year. These observational-based DMC per unit area values are shown in Figure
305 6, alongside BA based values reported in GFED4.1s for 2019 at 0.25° resolution. Total carbon emissions can be easily calculated using the assumed carbon fraction of vegetation (taken typically as 50±5%) (Andreae, 2019). Focusing in on a 4° ´ 4° region of Angola (Figure 7) demonstrates the far higher spatial detail of the FREM-derived DMC per unit area data compared with that provided by the modelling used within GFED.

https://doi.org/10.5194/acp-2022-193
Preprint. Discussion started: 25 April 2022

Atmospheric Chemistry and Physics Discussions

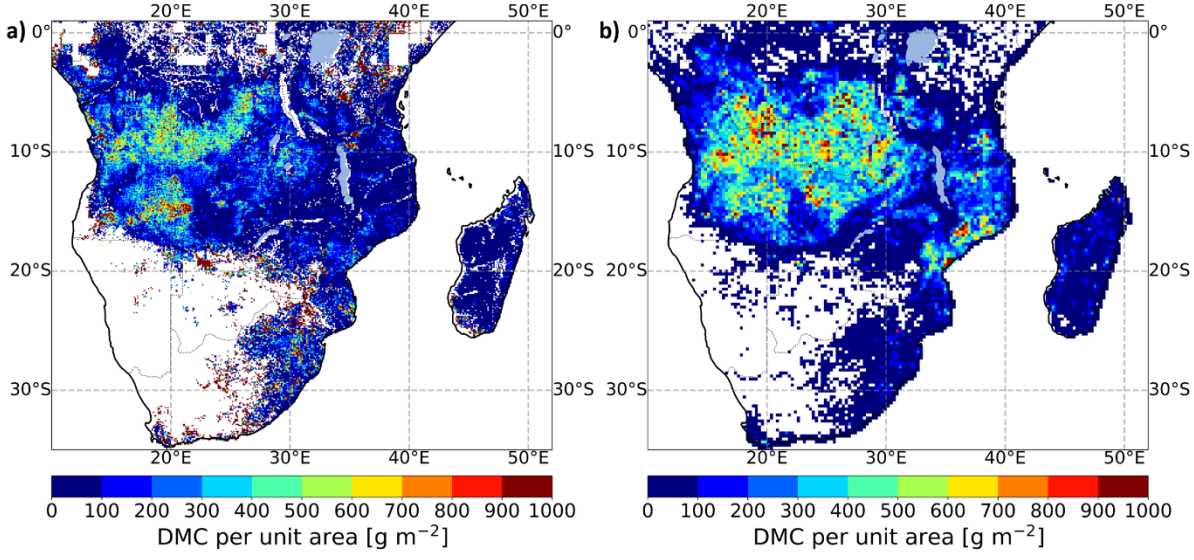

310

Figure 6 Dry matter consumed (DMC) per unit area, mapped across southern hemisphere Africa for 2019. (a) as calculated in 0.1° grid cell resolution by dividing the FREMs_bCO CO values (with SF correction) by the 20m FireCCISFD burned area product generated from Sentinel-2 MSI observations, and (b) as reported in GFED4.1s at 0.25° grid cell resolution.

315

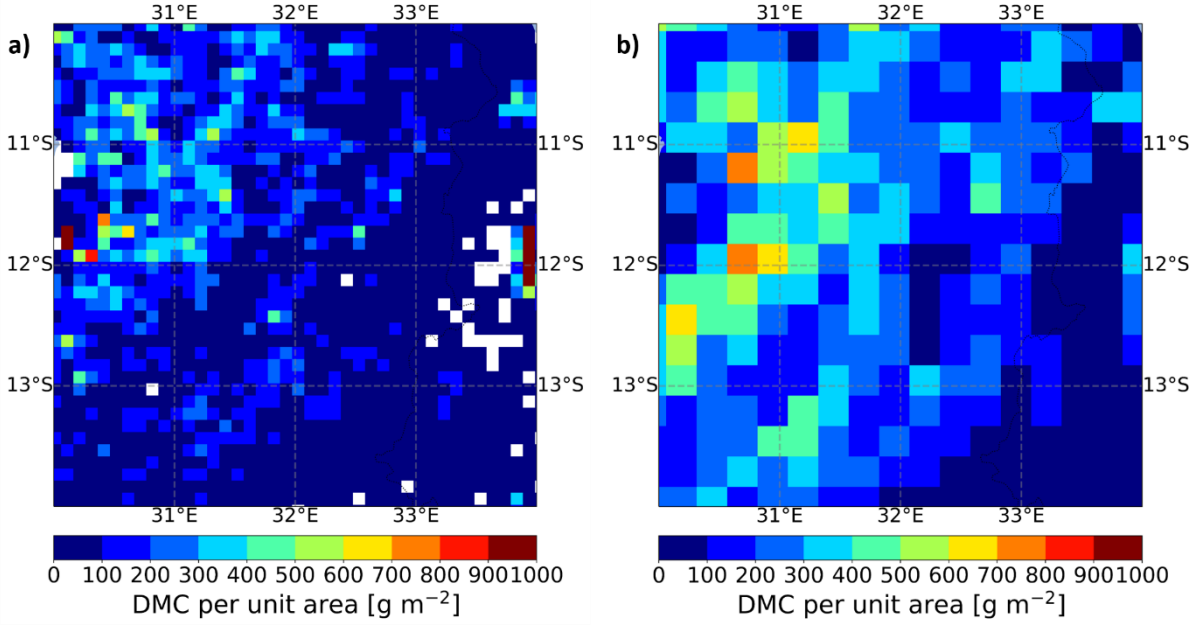

Figure 7. Mapped dry matter consumed (DMC) per unit area, calculated (a) at a 0.1° grid cell scale using the FREMs_bCO CO values (with SF correction) across a 4° × 4° region of Angola for the year 2019 and (b) the same DMC per area values for GFED4.1s.

https://doi.org/10.5194/acp-2022-193
Preprint. Discussion started: 25 April 2022


Atmospheric Chemistry and Physics Discussions

320 # 4 FREM-Derived CO Emissions Validation

4.1 Evaluation Methodology

Beyond the comparisons to GFEF4.1s detailed in Section 3, our FREMs_bCO emissions were further evaluated through their use in chemical transport model (CTM) simulations conducted with the Advanced Research Weather Research and Forecasting model (WRF-ARW v4.1.1; (Skamarock et al., 2019) and the Community Multiscale Air Quality model (CMAQ v5.3; (EPA,
325 2019); https://www.epa.gov/cmaq). The resulting model output fields were compared to Sentinel-5P TROPOMI TCCO observations that are completely independent of those used in the FREM emissions coefficient generation (i.e. those used within Figure 2). WRF-CMAQ is commonly used in operational AQ systems (Kukkonen et al., 2012) and in research related to fire emissions and smoke-contaminated air (Cheng et al., 2014; Baldassarre et al., 2015; Hu et al., 2016; Vongruang et al., 2017; Koplitz et al., 2018; Choi et al., 2019).

330

Model runs were conducted over the ~ 3000 km^2 region of SHAF shown in Figure 8a. Further regions of interest (ROIs) were used in comparisons between the WRF-CMAQ output and satellite CO observations. The WRF-CMAQ domain had a spatial resolution of 9 km, with 35 vertical model layers over a 347 × 319 grid. Model runs were conducted for the period 15th June to 29th August 2019 and were carried out in two separate simulations each initialised and fed with initial and boundary
335 conditions from a global meteorological (FNL; https://rda.ucar.edu/datasets/ds083.2/) and chemistry (WACCM; https://www2.acom.ucar.edu/gcm/waccm) model. The first half of June was excluded due to a change in the version of the global metrological model used as input. The second simulation was started from 29th July 2019 and both simulations featured a 24-hour spin-up time. The model configuration and set of physical schemes used in WRF were selected based on previous AQ simulations over SHAF using the WRF-Chem model (Kuik et al., 2015; Yang et al., 2013; Zhang et al., 2014). Details of
340 the WRF-CMAQ configuration and setup are summarised in Appendix B. Anthropogenic emissions were taken from the EDGAR-HTAPv2 inventory (https://edgar.jrc.ec.europa.eu/dataset_htap_v2), whilst biogenic and dust emissions were generated inline by the model. Emission coefficients for all gas species used were calculated through the application of Equation 1 with CO as the reference species. These emission coefficients were then multiplied by hourly mean SEVIRI FRP to generate all the fire-emitted gas and particulate species emissions used as input in the model. Aerosol species emissions
345 were generated through an analogues application of the updated FREM-TPM emission coefficients of Nguyen & Wooster (2020) (see Appendix A)

The modelled TCCO values (g.m^{-2}) were compared to Sentinel-5P TCCO observations from June to August 2019 – none of which were used in the C_e^{CO} derivation of Section 2.3. Sentinel-5P acquisitions over the model domain occur daily between ~
350 12:00 and 14:00 UTC, and the resulting TCCO retrievals were combined and compared with the mean CMAQ-derived TCCO from the same two-hour period. Both modelled and observed CO were mapped to a 0.1° grid and their degree of agreement quantified using the Pearson's correlation coefficient (r) and the normalised mean bias function (NMBF) described by (Yu et

https://doi.org/10.5194/acp-2022-193
Preprint. Discussion started: 25 April 2022

Atmospheric Chemistry and Physics Discussions

al., 2006). The NMBF has been specifically developed for comparing modelled and observed air pollutant concentrations, and it reduces the inflation in bias that may be caused by low values of the observed quantities (see Yu et al., 2006). NMBF is defined as:

$$NMBF = \frac{(\sum M - \sum O)}{|\sum M - \sum O|} \cdot \left[exp\left(\left| ln \frac{\sum M}{\sum O} \right| \right) - 1 \right] \qquad [2]$$

where M and O are the modelled and observed TCCO concentrations. As defined above, a positive NMBF indicates an overestimation of the model by a factor of 1 + NMBF, while a negative NMBF indicates that the model underestimates observations by a factor of (1-NMBF). Hence, a NMBF value of 0.10 is a 10% overestimation by the model, and -0.10 a 10% underestimation.

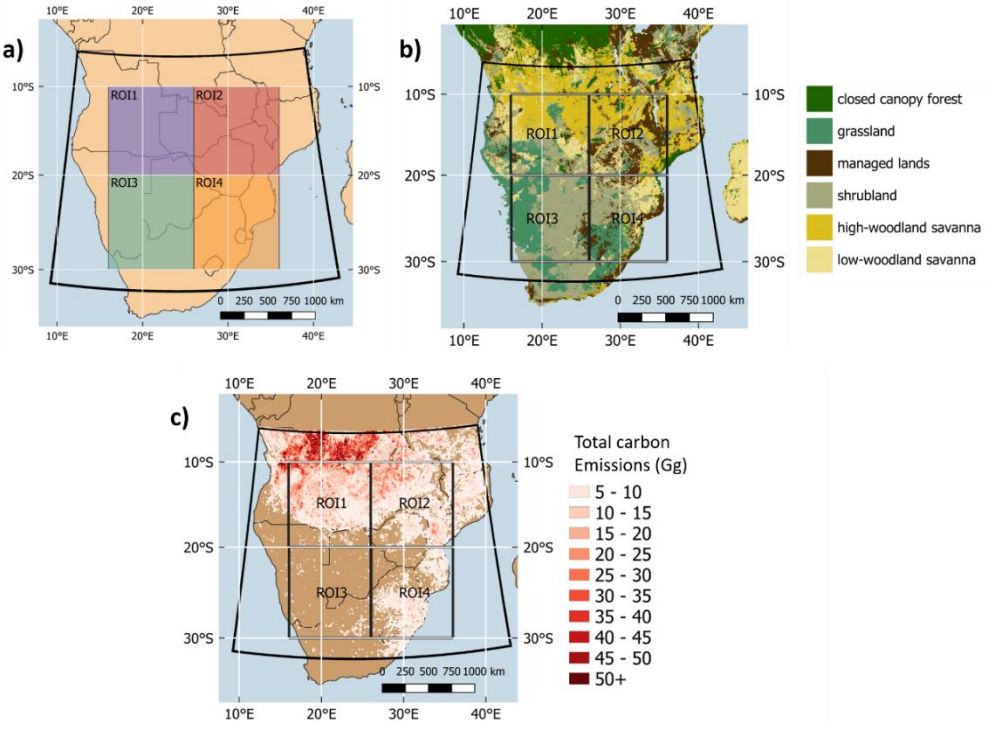

Figure 8. Southern hemisphere Africa (SHAF) model domain in WRF-CMAQ, fed with the FREM-derived landscape fire CO emissions inventory developed herein. Boxes indicate four smaller regions of interest (ROIs) used in comparisons of model output to satellite-derived CO observations. (a) Domain and ROIs, (b) spatial distribution of the six fire-affected biomes defined herein, and (c) spatial distribution of fire emitted total carbon released between 15th July and 29th August as estimated from the FREM-derived fire emissions inventory used as input to the CMAQ model.

https://doi.org/10.5194/acp-2022-193
Preprint. Discussion started: 25 April 2022

Atmospheric Chemistry and Physics Discussions

4.2 Evaluation Results

Mapped mean monthly TCCO as derived from the CMAQ modelling and Sentinel-5P TCCO (S5P hereafter) observations are shown in Figure 9, along with their percentage difference. In general, their spatial distribution agrees well - with the highest TCCO values in the northwest of the domain – which is the area with greatest fire activity (Figure 8). The magnitude of TCCO over this region in the CMAQ model output is however higher than that of the S5P observations, around 50% in some areas in June and July. Across the majority of the rest of the domain however, modelled TCCO is between 1% and 30% lower than observed TCCO. An improved agreement is seen in August, with the degree of over and underestimation of CMAQ CO compared to S5P generally reduced.

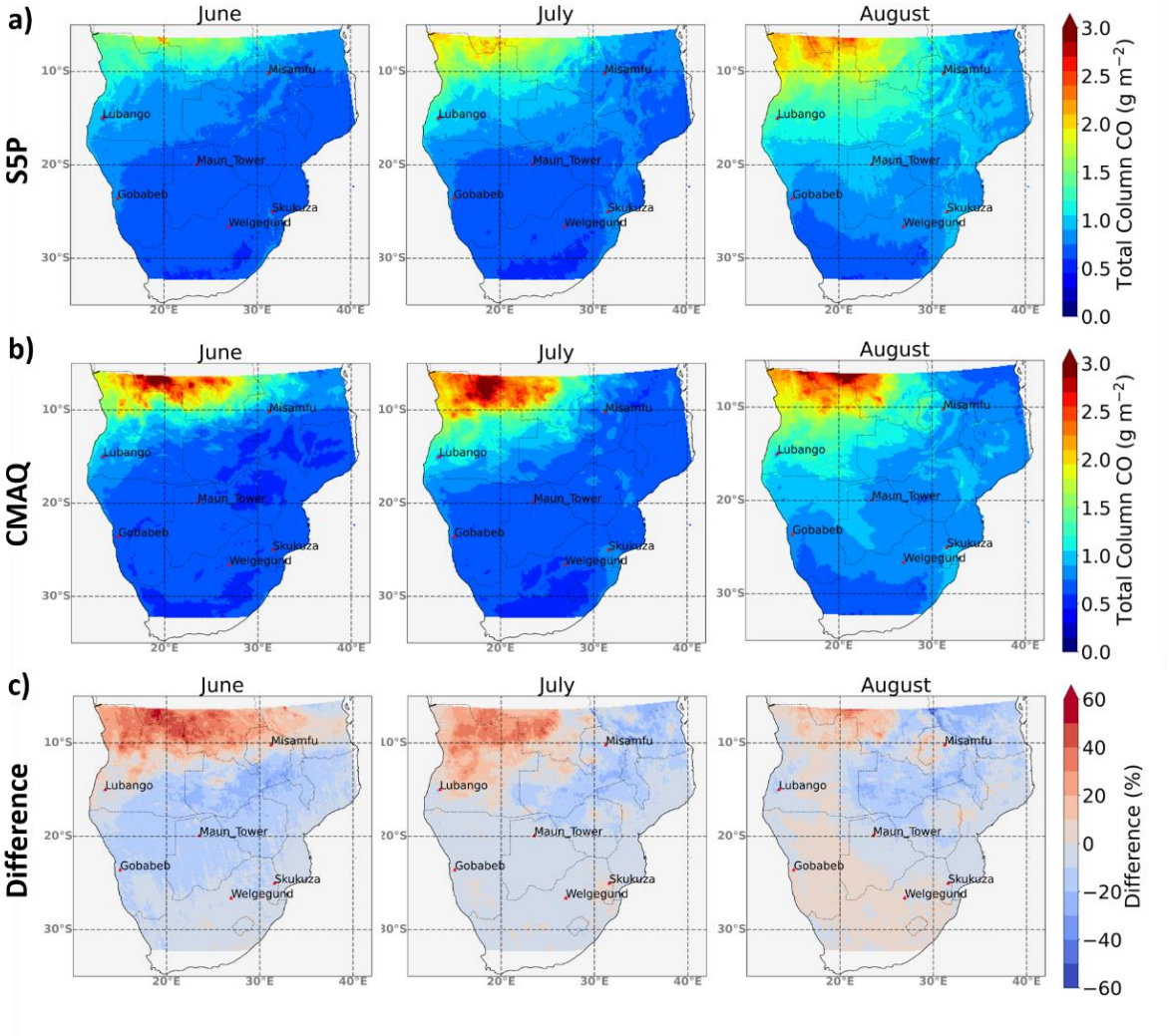

Figure 9. Mapped mean monthly total column carbon monoxide (TCCO) between 15th June and 29th August 2019, as determined by (a) S5P observations and (b) CMAQ modelling fed with the FREMs_bCO emissions inventory developed herein. Their percentage difference is shown in (c).

https://doi.org/10.5194/acp-2022-193
Preprint. Discussion started: 25 April 2022


Atmospheric Chemistry and Physics Discussions

Timeseries of modelled and observed daily summed TCCO (Gg) within the full domain extent and within ROI1 and ROI2 (labelled in Figure 8) are shown in Figure 10, along with direct comparisons of daily summed TCCO measures. Summed TCCO temporal patterns observed by S5P are well replicated in the CMAQ modelling, indicating that (i) temporal trends in active fires are being well captured in the SEVIRI FRP-PIXEL product and (ii) the meteorological fields of WRF, particularly wind, are performing well. In direct comparisons between daily summed TCCO across the four ROIs, ROI1 shows the best agreement between model and observations (NMBF = -0.01; a 1% underestimation by CMAQ compared to S5P). Mean daily summed TCCO for each ROI in each month of the CMAQ simulation period are summarised in

Table 3, along with statistics for the comparisons made within each region and month. In the three other ROIs, NMBF lies between -0.02 and -0.09 for direct CMAQ-S5P comparisons, and both the full domain and all ROIs show a strong correlation between modelled and observed CO (all $r \geq 0.81$).

https://doi.org/10.5194/acp-2022-193
Preprint. Discussion started: 25 April 2022

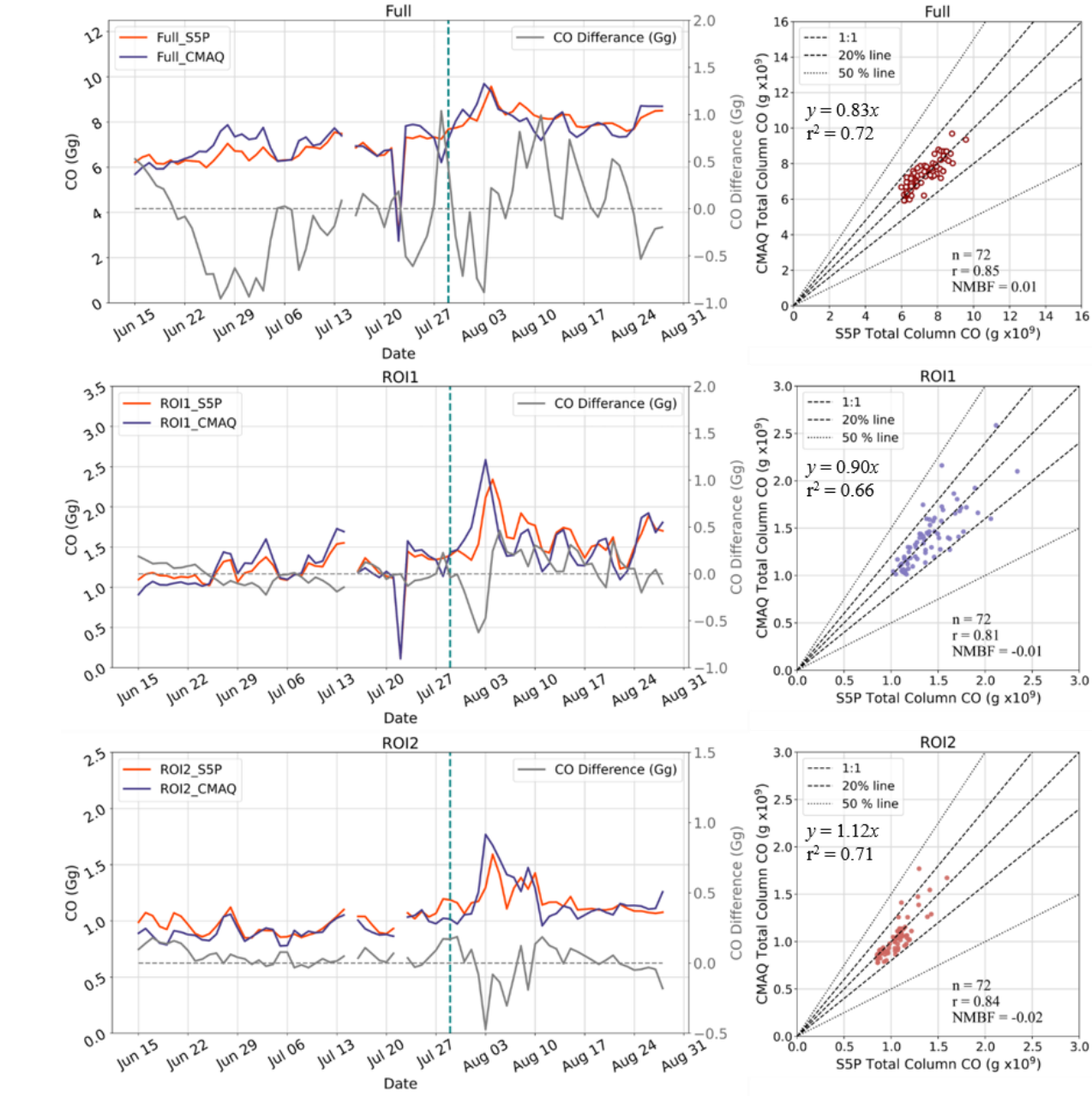

Figure 10. Results from the comparison of modelled (CMAQ) and observed (S5P) total column CO (TCCO) across the domain and two of the regions of interest (ROI) defined in Figure 8. (right-hand column) time series of daily summed TCCO over the full domain and the two ROIs as determined by CMAQ and S5P, with their difference represented by the solid grey line and the vertical dotted line at 29th July indicating the start of the second simulation (see main text). (left-hand column). Scatterplot comparing the daily summed TCCO in the right hand column plots from CMAQ and S5P. The Pearson's correlation and NMBF of the dataset are shown, along with dotted lines indicating the 1:1, ±20% and ±50% relationships. The NMBF of 0.04 indicates a mean 4% overestimation by the model compared to the observations. Results from the comparisons plotted here are summarised

https://doi.org/10.5194/acp-2022-193
Preprint. Discussion started: 25 April 2022

Atmospheric Chemistry and Physics Discussions

Table 3. Monthly mean summed TCCO (Gg), as derived across the SHAF domain of Figure 8 from S5P observations and from the CMAQ model output fed with the FREMs_bCO CO emissions. The same values for the four regions of interest (ROI) indicated in Figure 8 are also shown, along with the NMBF and Pearson's correlation coefficient metrics. An NMBF of e.g. 0.05 indicates a mean 5% overestimation of the modelled values compared to the observations.

		CMAQ Mean TCCO (Gg)	S5P Mean TCCO (Gg)	NMBF	Pearson's Correlation coefficient
Full Domain					
	June	6.70	6.39	0.05	0.69
	July	7.21	7.01	0.03	0.75
	August	8.12	8.24	-0.01	0.70
	All	7.44	7.35	0.01	0.85
ROI1					
	June	1.14	1.16	-0.01	0.79
	July	1.36	1.31	0.04	0.83
	August	1.59	1.65	-0.04	0.67
	All	1.40	1.41	-0.01	0.81
ROI2					
	June	0.89	0.97	-0.09	0.72
	July	0.95	0.99	-0.04	0.83
	August	1.21	1.19	0.02	0.72
	All	1.04	1.06	-0.02	0.84
ROI3					
	June	0.88	0.97	-0.10	0.88
	July	1.02	1.11	-0.09	0.89
	August	1.24	1.33	-0.08	0.61
	All	1.07	1.16	-0.09	0.77
ROI4					
	June	0.73	0.78	-0.08	0.84
	July	0.80	0.82	-0.04	0.85
	August	0.92	0.94	-0.02	0.87
	All	0.83	0.86	-0.03	0.90

https://doi.org/10.5194/acp-2022-193
Preprint. Discussion started: 25 April 2022


Atmospheric Chemistry and Physics Discussions

CMAQ-modelled and S5P-observed TCCO were also compared for individual smoke plumes. A total of 383 plumes (see Figure 11a) were manually identified via visual inspection of the S5P TCCO product between 15th July and 29th August 2019 and defined using polygons which were then matched to the CMAQ model output at 0.1° resolution. In some cases the spatial distribution of individual plumes in the S5P TCCO product and the CMAQ TCCO output differed slightly – mainly due to differences in the modelled wind direction/speed and the real wind fields. Therefore, a 0.1° buffer was added around each validation plumes' polygon to account for these variations. In the region of highest fire activity (in the north-west region of the model domain) relatively few CO plumes were identified, however, since the S5P TCCO measures were consistently high across this region and individual plumes could not be easily distinguished in the S5P TCCO product. For all identified plumes, in-plume CO was calculated for both model and observation as the summed TCCO present within the bounding polygon containing the plume in each dataset.

Figure 11b shows the relationship derived between the CMAQ-modelled and S5P-observed in-plume CO. Compared to daily total TCCO over the full domain (Figure 10; NMBF = 0.01), in-plume NMBF is slightly higher at 0.04, i.e. a 4% overestimation of the modelled data compared to the observations, while the Pearson's corelation increases from 0.85 to 0.89. The slope of the line-of-best fit to for this data is 1.05 and with an r^2 of 0.80. Figure 11b shows that the plumes with the highest TCCO values (in both the S5P product and in the CMAQ model) also tend to have a higher total CO in CMAQ than in S5P. This is less true for plumes with TCCO below 20 Mg - indicating that the appropriateness of the small fire correction applied, unsurprisingly, depends on the size of the fire i.e. – the FRP contribution from small fires undetected in the SEVIRI product. The time-series of daily mean in-plume CO (Figure 11c) shows that the difference between these measures does not vary significantly by month.

https://doi.org/10.5194/acp-2022-193
Preprint. Discussion started: 25 April 2022

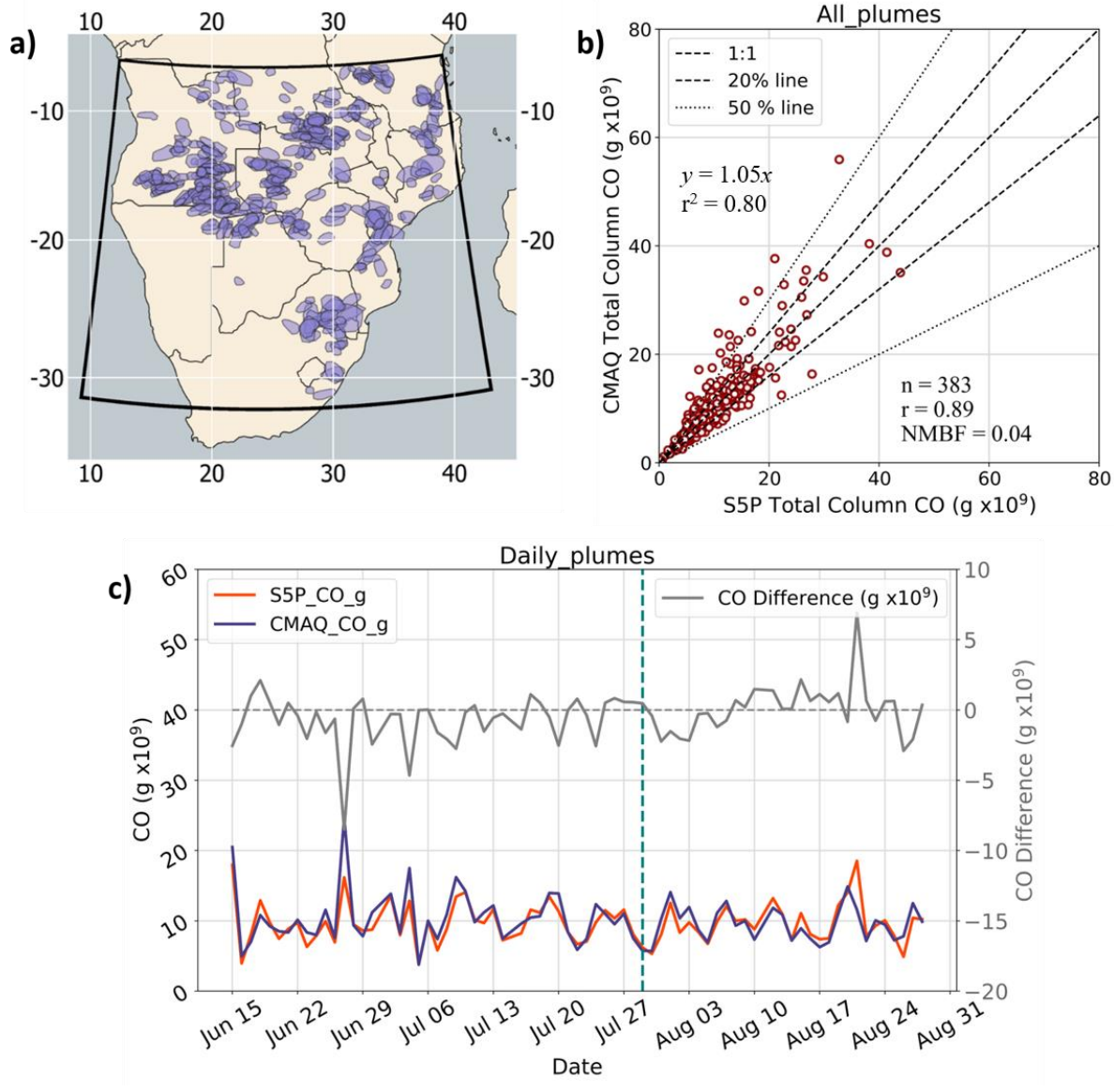

Figure 11. Evaluation of FREM-derived CO emissions based on WRF-CMAQ modelling. (a) Model domain and the bounding polygons of 383 plumes identified in the Sentinel-5P (S5P) total column carbon monoxide (TCCO) product between 15th June and 29th August 2019 used in the evaluation. (b) Relationship between modelled and observed TCCO for the individual smoke plumes identified in (a). The Pearson's correlation and NMBF of the dataset are shown, along with dotted lines indicating the 1:1, ±20% and ±50% relationships. The NMBF of 0.04 indicates a 4% mean overestimation by the model compared to the observations. (c) Daily summed TCCO of all plumes observed on each day of the simulation as determined by CMAQ (purple) and S5P (red), with their difference represented by the grey line (right hand side y-axis). The vertical dotted line on 29th July indicates the start of the second simulation period (see main text).

https://doi.org/10.5194/acp-2022-193
Preprint. Discussion started: 25 April 2022


Atmospheric Chemistry and Physics Discussions

5 Summary and Conclusions

We have developed a significant advance to the 'Fire Radiative Energy Emissions' (FREM) landscape fire emissions methodology of Mota and Wooster (2018) and Nguyen and Wooster (2020), namely the extension to directly relate CO emission rates to FRP observations using an emissions coefficient [C_e^{CO}] derived from satellite total column CO (TCCO) and FRE measures. Using 277 matchup fires distributed across northern and southern hemisphere Africa, we have generated C_e^{CO} values [g.MJ^{-1}] for six fire-affected biomes which directly link emission rates of CO (g.s^{-1}) to FRP (MW). We have applied these coefficients to a 16-year geostationary FRP dataset of African landscape fires to generate the highest spatio-temporal resolution African CO fire emissions inventory currently available. We find our CO emissions totals to be similar to those of the most recent version of the 'bottom-up' Global Fire Emissions Database (GFEDv4.1s; van der Werf et al., 2017), particularly across SHAF where they are almost identical in magnitude, though featuring a slightly earlier peak in monthly CO emissions coming from FREM compared to GFED.

Since direct validation of large-scale fire emissions estimates remains unfeasible, we have conducted an evaluation of the FREM-derived CO emissions via their use within the WRF-CMAQ atmospheric chemical transport model across a southern African domain. The generated regional-scale total column CO (TCCO) concentration fields are then compared to independent TCCO observations coming from Sentinel-5P TROPOMI. Results of this validation indicate very good agreement between the modelled and observed TCCO values in general, with a bias of 0.01 and 0.04 (1% and 4% mean overestimation by the model compared to observations) over the full model domain and over individual fire plumes respectively. CO emissions are overestimated to a greater extent (by up to around 50%) in the north-west region of the domain where high fire activity is observed, and where CO from fires outside the domain maybe being transported into the model domain. The slope of a linear best fit relationship between S5P CO and CMAQ CO within individual fire-generated plumes was 1.05 with an r^2 of 0.80. In comparison to the ~30% average difference observed between GFEDv3 CO emissions and MOPITT CO observations (Pechony et al., 2013) the results of the evaluation herein show good agreement and are well within the range of biases observed in similar evaluations of other fire emissions inventories (Chevallier et al., 2009; Ichoku and Ellison, 2014; Kaiser et al., 2012; Kopacz et al., 2010; Reddington et al., 2016). The FREM-derived CO emissions produced were used to calculate estimates of Dry Matter Consumed (DMC) and DMC per unit area for 2019. The former through use of CO emission factors and the latter through an inversion of the approach of Seiler and Crutzen (1980) in which BA data comes from the 20 m FireCCISFD product of (Roteta et al., 2019). DMC measures produced via FREM-derived CO emissions introduce less uncertainty than those produced from the FREM-TPM emissions of Nguyen and Wooster (2020) (updated in Appendix A) due to CO emission factors being far less variable than TPM emission factors in general, especially from fires in tropical forests and cultivated land (Akagi et al., 2011; Andreae, 2019).

https://doi.org/10.5194/acp-2022-193
Preprint. Discussion started: 25 April 2022


Atmospheric Chemistry and Physics Discussions

Future developments to the approach developed herein will include its application to FRP data from other geostationary satellites, for example those from Himawari (Xu et al., 2017), Meteosat Indian Ocean and GOES (Xu et al., 2010). Emissions of other gases can be derived from the ratio of their emissions factors to those of CO, and this overall approach forms the basis of a new fire emissions product to be delivered by the EUMETSAT Land Surface Analysis Satellite Application Facility (http://landsaf.meteo.pt).

6 Appendices

6.1 Appendix A

To maintain a consistent methodology between the FREM CO-based fire emissions inventory described in this work and the TPM-based version described in Nguyen and Wooster (2020) which was derived using Orthogonal Distance Regression (ODR), the OLS regression approach used herein was re-applied to the fire-plume match-up dataset of Nguyen and Wooster (2020). Updated FREM TPM-based fire emissions coefficients [C_e^{TPM}] were generated from the nearly 1000 sample fires detailed in Nguyen and Wooster (2020). Each matchup consisted of a set of SEVIRI FRP-PIXEL product AF pixels for the target fire, along with the 1 km MCD19A1 MAIAC AOD product for that fire (see Nguyen and Wooster (2020) for details). Figure A1 shows the updated TPM emissions coefficients [C_e^{TPM}] for each of the six biomes defined herein, and these are summarised in Table A1Table (Col 1) along with the previous ODR-derived values of Nguyen & Wooster (2020; Col 2) and various other forms of the same coefficients.

https://doi.org/10.5194/acp-2022-193
Preprint. Discussion started: 25 April 2022

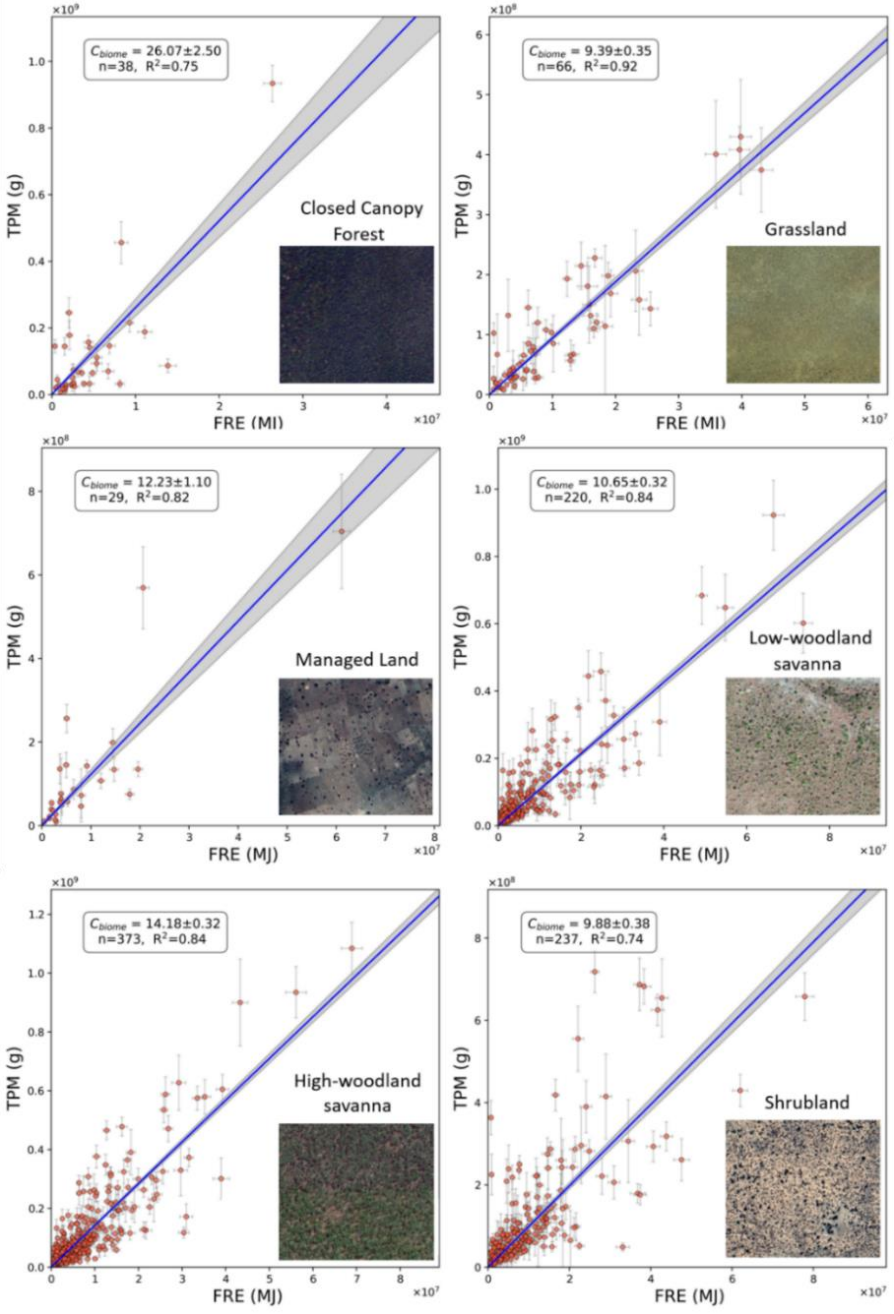

Figure A1. TPM Smoke emission coefficients (C_e^{TPM}; in g.MJ-1) for the six African fire-affected biomes defined in the main manuscript, each derived from the slope of an ordinary least-squares (OLS) regression between data of fire-emitted total particulate matter (TPM) and matching fire radiative energy (FRE). The grey shaded area defines the 95% probability prediction interval of the OLS-derived slope. Each scatterplot is accompanied by an illustrative insert that depicts the typical landcover for the biome as seen in ©Google Earth (example locations are Closed Canopy Forest 10.359° S, 19.086° E; Grassland 21.180° S, 19.560° E; Managed Land 10.495° N, 7.586° E; Low-Woodland Savanna 7.085° N, 27.095° E, High-Woodland Savanna 12.523° S, 23.323° E and Shrubland 23.055° N, 22.242° E).

https://doi.org/10.5194/acp-2022-193
Preprint. Discussion started: 25 April 2022

Atmospheric Chemistry and Physics Discussions

Table A1. TPM emission coefficients from previous FREM versions and updates (in units of g.MJ^{-1})

	FREM C_e^{TPM} (OLS updated)	FREM C_e^{TPM} (ODR; Nguyen and Wooster, 2020)	FREM C_e^{TPM} (Mota & Wooster, 2018)	FREM C_e^{TPM} (from C_e^{CO} of Figure 2 and Equ 1)	FEER- Equivalent (see Nguyen and Wooster, 2020)
Closed canopy Forest	26.07	34.33	65.63	16.43	16.34
Managed land	12.23	13.98	15.62	15.00	15.80
Grassland	9.39	9.99	13.03	9.52	10.98
Shrubland	9.88	12.17	17.36	10.22	10.97
Low-woodland savanna	10.65	12.10	19.75	10.78	12.78
High-woodland savanna	14.18	16.43	19.75	10.32	13.81

https://doi.org/10.5194/acp-2022-193
Preprint. Discussion started: 25 April 2022


Atmospheric Chemistry and Physics Discussions

6.2 Appendix B

Table B1. Summary of WRF-CMAQ model configuration

General features	
Domain extent	10°E - 44 °E, 5°S -32°S
Modelled time period	15th June to 28th July, and 29st July to 29st Aug 2019
Resolution	9 km × 9 km, 35 vertical levels (top layer at 5 kPa)
WRF configuration	**Scheme**
cloud microphysics	Lin et al.
radiation (shortwave)	Goddard
radiation (longwave)	Rapid Radiative Transfer Model (RRTM)
boundary layer physics	Mellor-Yamada-Janic (MYJ)
land surface processes	Noah LSM
cumulus convection	Grell 3-D
CMAQ configuration	
Chemistry mechanism	CB6r3
aerosol module	AERO7
Dust emissions	inline
Biogenic emissions	inline BEIS3
Initial and boundary conditions	
Metrology	NCEP FNL, 0.25° × 0.25°, 26 levels, 6 hour
Chemistry	WACCM, 0.9° × 1.25°, 88 levels, 3 hour

6.3 Appendix C

The updated TPM emissions coefficients [C_e^{TPM}] calculated in Appendix A (with the exception of the closed canopy forest value) were used to derive an emission inventory for aerosols that was then used as an input to a WRF-CMAQ simulation. These same simulations used gaseous emissions generated from the FREMs_bCO emissions coefficients described in the main article as input. To evaluate the TPM emissions values, the AOD fields produced by these CMAQ simulations were compared with independent ground based and satellite-based AOD metrics. The WRF-CMAQ model set-up and configuration are described in Appendix B and in the main article, while the results of the FREM-TPM emissions estimates evaluation are presented in here.

https://doi.org/10.5194/acp-2022-193
Preprint. Discussion started: 25 April 2022

Atmospheric Chemistry and Physics Discussions

AERONET is a global network of ground-based sun photometers that provides retrievals of aerosol optical properties, including Angström exponent, aerosol refractive index, and aerosol optical depth (AOD) at different wavelengths (Holben et al., 2001). Data from AERONET sites within the CMAQ model domain were used in comparisons with CMAQ-generated AOD fields (at 381nm). The AERONET sites used were: Maun Tower (19.9°S, 23.55°E), Lubango (15.0°S, 13.4°E), Misamfu (10.2°S, 31.2°E), Gobabeb (23.6°S, 15.0°E), Welgegund (26.6°S, 26.9°E) and Skukuza (35.0°S, 31.6°E). AERONET AOD data is available for the full simulation period from each of these sites, with the exception of Misamfu and Welgegund that have data available from 15th June until 29th July and 13th August respectively. AERONET AOD observations at 380 nm are used in comparisons to WRF-CMAQ modelled AOD at 381 nm.

Figure C1 shows hourly mean AOD, averaged across all six AERONET sites, as determined by CMAQ and by the AERONET measurements. CMAQ AOD captures the temporal pattern of AOD rather well across these six sites, but in general tends to show higher values than the ground-based measures. Hourly modelled and observed AOD were compared in terms of their Pearson's correlation (r) and NMBF in each month as well as over the full simulation period, and these results are summarised in Table C1 along with monthly mean AOD for CMAQ and AERONET at each site. NMBF over the full simulation period at the six AEONET sites ranges between a 4% underestimation and 41% overestimation by CMAQ relative to AERONET, and the Pearson's correlation coefficient ranges between 0.36 and 0.72.

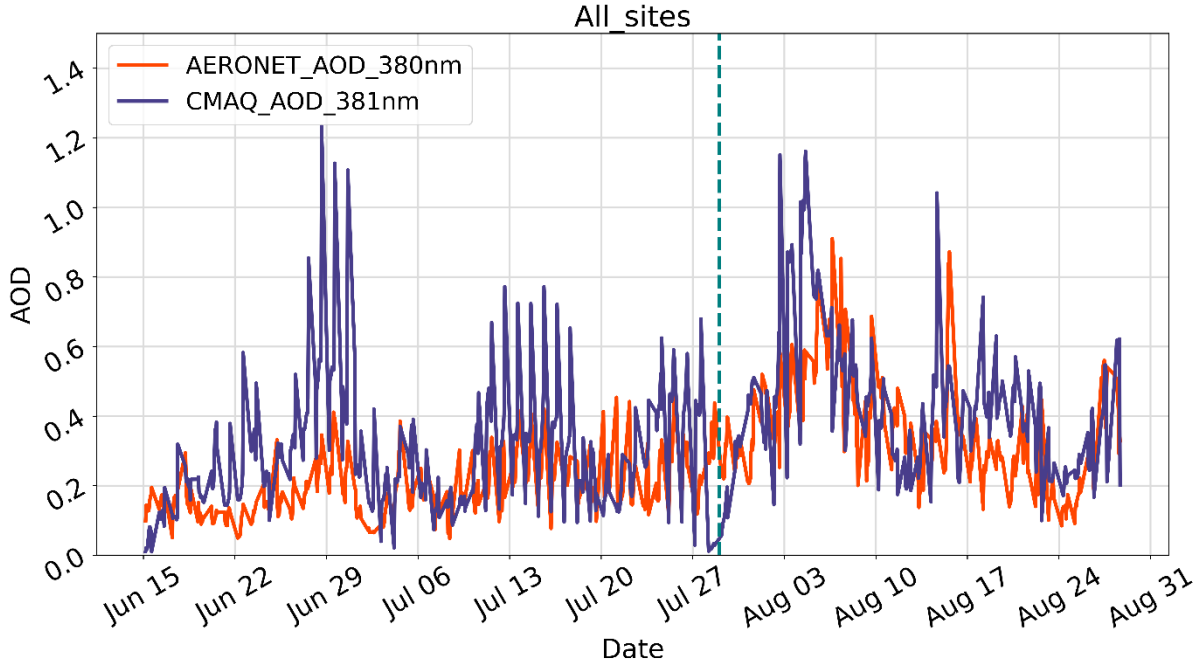

Figure C1 Hourly AOD averaged over all six AERONET sites, both from the CMAQ simulations and AERONET observations. A vertical dotted line on 29th July indicates the start of the seconds simulation.

https://doi.org/10.5194/acp-2022-193
Preprint. Discussion started: 25 April 2022

Atmospheric Chemistry and Physics Discussions

Table C1 Monthly mean of hourly CMAQ and AERONET AOD, the NMBF of hourly CMAQ AOD with respect to observations and the temporal Pearson's correlation coefficient of hourly AOD over each month and the whole modelled period (15th June to 29th August 2019).

	Month	CMAQ Mean	AERONET Mean	NMBF	Pearson's Correlation (r)
Lubango	June	0.52	0.26	1.00	0.71
	July	0.68	0.49	0.65	0.70
	August	0.66	0.56	0.16	0.42
	All	0.64	0.45	0.41	0.50
Misamfu	June	0.41	0.13	2.08	0.72
	July	0.20	0.22	-0.70	0.16
	All	0.27	0.19	0.47	0.13
Gobabeb	June	0.22	0.17	0.34	0.75
	July	0.20	0.25	-0.30	0.60
	August	0.21	0.24	-0.11	0.13
	All	0.21	0.22	-0.03	0.45
Maun Tower	June	0.06	0.10	-0.55	0.57
	July	0.12	0.12	-0.04	0.69
	August	0.40	0.39	0.05	0.61
	All	0.21	0.22	0.00	0.72
Welgegund	June	0.13	0.12	0.10	0.57
	July	0.13	0.11	0.31	0.50
	August	0.52	0.45	0.14	0.29
	All	0.21	0.18	0.21	0.66
Skukuza	June	0.27	0.21	0.26	0.53
	July	0.36	0.25	0.43	0.19
	August	0.43	0.40	0.08	0.41
	All	0.37	0.29	0.27	0.39
All Sites	June	0.28	0.16	0.78	0.64
	July	0.28	0.22	0.27	0.33
	August	0.44	0.37	0.20	0.53
	All	0.34	0.26	0.31	0.59

https://doi.org/10.5194/acp-2022-193
Preprint. Discussion started: 25 April 2022


Atmospheric Chemistry and Physics Discussions

In addition to this comparison to ground-based AOD data, CMAQ modelled AOD at 550 nm was compared to the MODIS MAIAC 550 nm 1 km product (Collection 6 MCD19A2; Lyapustin et al., 2018) - the same AOD product used in the derivation of FREMv2 TPM emissions coefficients (Appendix A and Nguyen and Wooster (2020)), though a completely different set of days were used in the generation of the matchup dataset. Daytime Aqua and Terra overpasses occurring between approximately 08:00 and 10:00 UTC daily over the CMAQ domain were compared to mean CMAQ AOD between 08:00 and 10:00 at 550 nm. Both modelled and observed AOD were remapped to a 0.1°×0.1° grid for ease of comparison.

The spatial distribution of monthly mean AOD in the MAIAC AOD product and CMAQ is shown in Figure C2. Most notable in Figure C2Figure is the large variation between under and over estimation by modelled AOD compared with MAIAC AOD, as can be seen in the difference plot of C2c. In the north west of the domain, where the highest fire activity occurs (See main article, Figure 8 c), some areas feature CMAQ AOD that is close to 60% greater than MAIAC AOD, with the highest overestimation occurring in June. While in other regions of the of the domain, CMAQ underestimates observed AOD significantly. In these areas, however, AOD values are already low and hence, this supposed underestimation is not as significant in absolute terms, though it does indicate that - in its base state - the CMAQ model tends to underestimate AOD.

https://doi.org/10.5194/acp-2022-193
Preprint. Discussion started: 25 April 2022

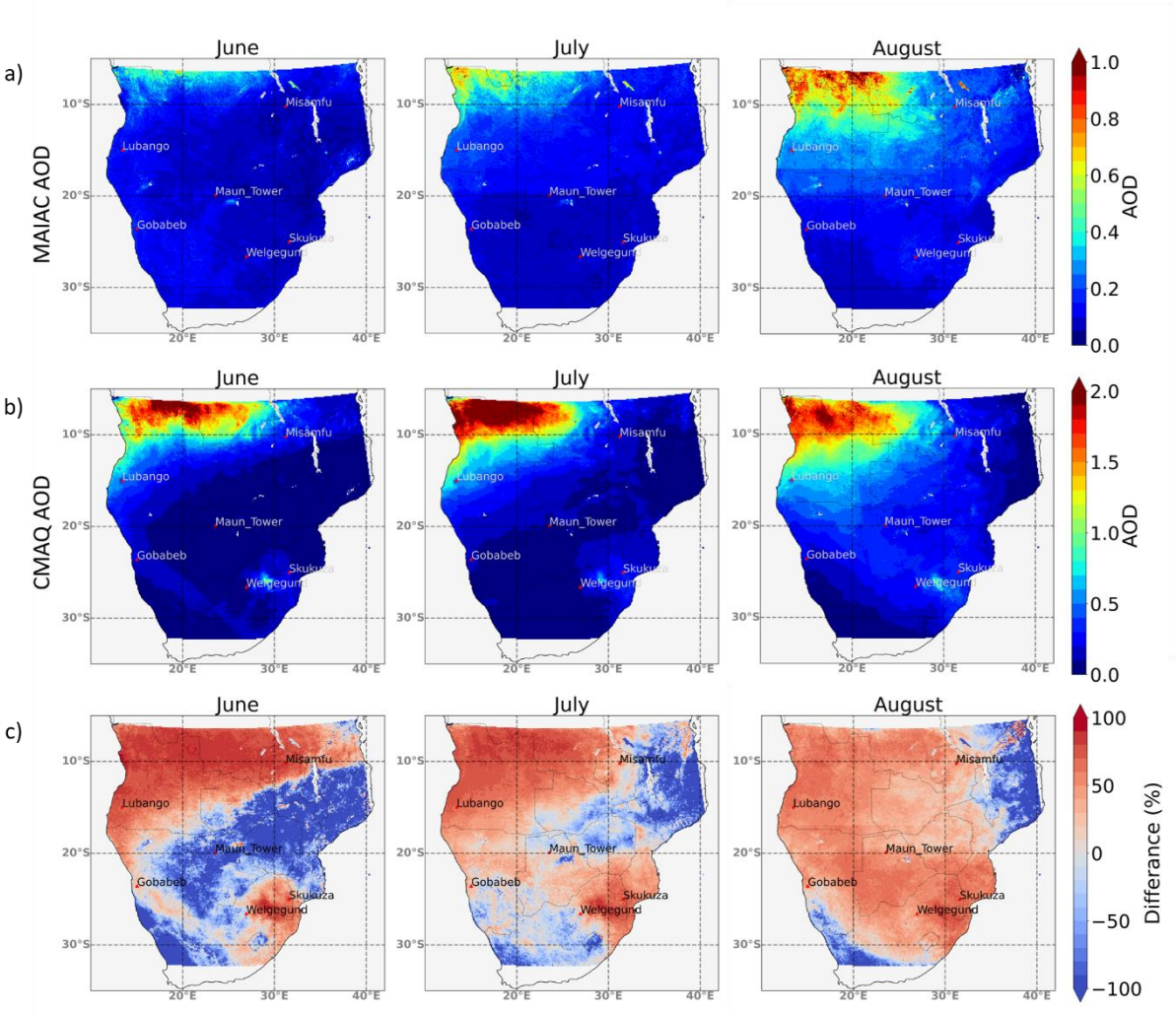

550

Figure C2. Mapped mean monthly AOD at 550 nm from a) the MAIAC satellite product and b) CMAQ simulations (note - colour scale differences between a) and b)) during the simulation period from 15th June to 29th August 2019. c) shows the percentage difference between MAIAC and CMAQ AOD

555 Daily modelled and observed AOD in each ROI (see main article Figure 8a) and in the full domain were used to generate mean monthly AOD during the simulation period (Table C2) and the NMBF and Pearson's correlation coefficient (r) between CMAQ and MAIAC daily AOD were also calculated. The results show that CMAQ AOD, in general, is significantly overestimated relative to MAIAC AOD, and this overestimation is far greater than for the CMAQ TCCO comparisons to Sentinal-5P TCCO shown in the main manuscript (4). Daily mean CMAQ AOD in the domain for the full simulation period
560 is 120% higher than MAIAC mean AOD, and when restricted to days in June this increases to 184%. Mean CMAQ AOD in ROI1 – which includes much of the area with the highest fire activity - shows the largest overestimation, ranging between

https://doi.org/10.5194/acp-2022-193
Preprint. Discussion started: 25 April 2022

Atmospheric Chemistry and Physics Discussions

105% and 180% depending on the month. Conversely ROI2 and ROI3, in which there is generally lower fire activity, show lower NMBF values ranging from an underestimation of 30% to an overestimation of 77% by CMAQ AOD. The correlation between modelled and observed daily means varies by ROI and by month, but in most cases r > 0.60.

565

Table C2. Monthly means of daily CMAQ and MAIAC AOD, in the full extent of the domain and the ROIs, the NMBF of daily CMAQ AOD with respect to observations and the temporal Pearson's correlation coefficient of daily AOD over each month and the whole modelled period are also included (15th June to 29th August 2019)

		CMAQ Mean AOD	MAIAC Mean AOD	NMBF	Pearson's Correlation (r)
Full Domain	June	0.11	0.04	1.84	0.77
	July	0.13	0.05	1.37	0.63
	August	0.15	0.79	0.94	0.21
	All	0.13	0.06	1.2	0.5
ROI1	June	0.26	0.09	1.8	0.9
	July	0.37	0.15	1.42	0.73
	August	0.55	0.27	1.05	0.48
	All	0.41	0.18	1.21	0.64
ROI2	June	0.07	0.09	-0.3	0.44
	July	0.07	0.07	0.06	0.69
	August	0.21	0.11	1	0.63
	All	0.13	0.09	0.42	0.64
ROI3	June	0.07	0.04	0.77	0.8
	July	0.11	0.09	0.16	0.79
	August	0.22	0.16	0.39	0.59
	All	0.14	0.1	0.32	0.73
ROI4	June	0.07	0.05	0.56	0.69
	July	0.11	0.05	0.97	0.46
	August	0.17	0.07	1.41	0.71
	All	0.12	0.06	1.13	0.81

570

https://doi.org/10.5194/acp-2022-193
Preprint. Discussion started: 25 April 2022

Atmospheric Chemistry and Physics Discussions

As with the evaluation conducted for the FREM-derived CO emissions (see main article Section 4), comparisons between CMAQ and MAAIC AOD were also conducted for individual smoke plumes identifiable in the MAIAC AOD product. Individual fire emitted plumes were identified in the MAIAC AOD product at its native 1 km spatial resolution. Polygons were used to define plume boundaries, and each plume was matched between modelled and observed AOD data. A 0.1° grid cell buffer was applied to account for variations in the spatial distributions of the plumes. Fire emitted AOD for CMAQ and MAIAC plumes were calculated via the method described in Nguyen & Wooster (2020).

Figure C3 shows the spatial distribution of the 415 individual smoke plumes used in comparisons and the relation between the fire emitted AOD fields of CMAQ and MAIAC for each of these plumes. There is a large spread in the data, and the Pearson's correlation is relatively low at 0.43. The NMBF indicates an overall underestimation of CMAQ AOD compared with MAIAC AOD, by 10%. This is drastically different from the 120% overestimation of daily AOD by CMAQ relative to MAIAC in the full domain comparisons. The impact of model error, and the more extensive spatial variability between the modelled and observed plumes, may significantly contribute to the large differences seen in the comparison made at large scales and those for individual plumes. The true accuracy of the FREM derived emission is likely somewhere in between.

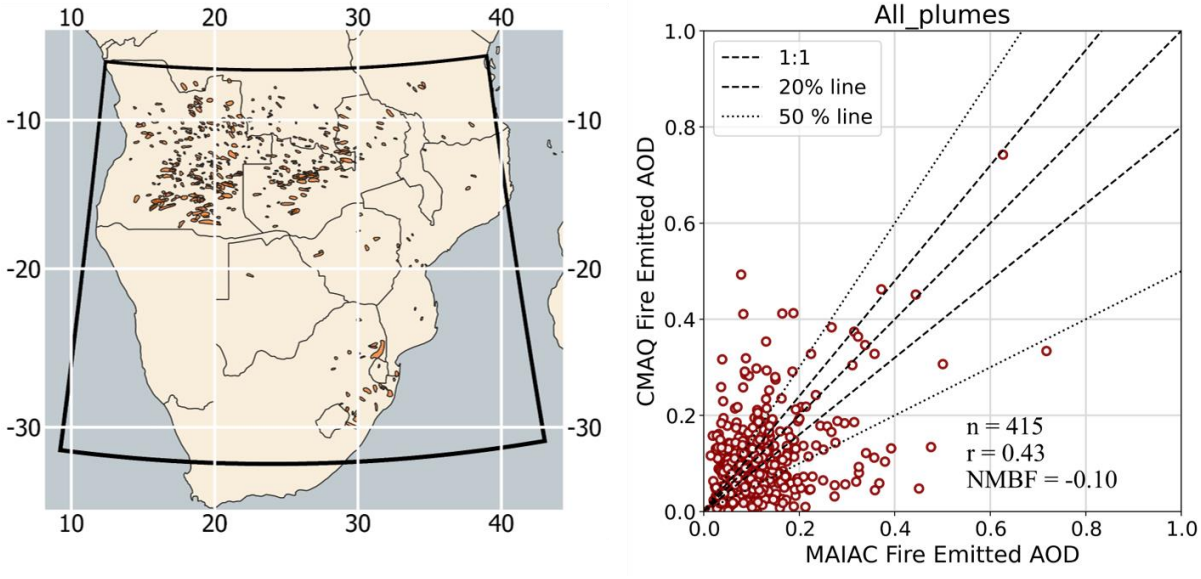

Figure C3 Location of smoke plumes identified in the MAIAC 1 km AOD product between 15th June and 29th August 2019 and the bounding polygons /used to define the area over these plumes (left). Relationship between fire-emitted CMAQ AOD and observed fire-emitted MAIAC AOD in these plumes (right), the Pearson's correlation and NMBF of the dataset is shown along with dotted lines indicating the 1:1, 20% and 50% lines.

https://doi.org/10.5194/acp-2022-193
Preprint. Discussion started: 25 April 2022


Atmospheric Chemistry and Physics Discussions

7 Code availability

Code is available upon request to Hannah Nguyen (hannah.nguyen@kcl.ac.uk)

8 Data Availability

The fire emissions inventory presented will available from the EUMETSAT Land Surface Analysis Satellite Application Facility (http://landsaf.meteo.pt) in the near future. Data can be provided upon request to Hannah Nguyen (hannah.nguyen@kcl.ac.uk) in the interim.

9 Author contributions

MW was responsible for conceptualization of methodology, and JP was responsible for the generation of the CO plume match-up dataset and emission coefficients. HN assisted on emissions methodology and was responsible for emission validation with WRF-CMAQ. MW and HN contributed to first draft and prepared initial visualisations. HN and MW were responsible for writing and editing the final manuscript.

10 Competing Interests

The contact author has declared that neither they nor their co-authors have any competing interests.

11 Acknowledgements

Sentinel-5P products are distributed freely by Copernicus Open Access Hub (https://scihub.copernicus.eu/), as is the SEVIRI FRP-PIXEL product of the EUMETSAT LAS SAF (https://landsaf.ipma.pt/) and VIIRS product of LAADS DAAC (https://ladsweb.modaps.eosdis.nasa.gov/). We would like to thank the LAS SAF and MODIS teams for the development and distribution of these products, as well as the developers and providers of FEER, GFAS, GFED, CCI Landcover, Landsat VCF and FireCCISFD11. Funding for this work was provided by EPSRC's Centre for Doctoral Training in Cross-Disciplinary Approaches to Non-Equilibrium Systems (CANES; EP/L015854/1), NERC National Capability funding to NCEO (NE/R016518/1), NERC Grant (NE/S014004/1) and by EUMETSAT's Satellite Applications Facility Programme which supports the Land Surface Analysis Satellite Application Facility (https://landsaf.ipma.pt/en/, LSA SAF CDOP-4) where the Meteosat FRP-PIXEL and FRP-GRID products are generated. We also thank the anonymous reviewers for their comments which have helped improve the quality and content of this manuscript.

https://doi.org/10.5194/acp-2022-193
Preprint. Discussion started: 25 April 2022


Atmospheric Chemistry and Physics Discussions

12 References

Abel, S. J., Haywood, J. M., Highwood, E. J., Li, J. and Buseck, P. R.: Evolution of biomass burning aerosol properties from an agricultural fire in southern Africa, Geophys. Res. Lett., 30(15), 10–13, doi:10.1029/2003GL017342, 2003.

Akagi, S. K., Yokelson, R. J., Wiedinmyer, C., Alvarado, M. J., Reid, J. S., Karl, T., Crounse, J. D. and Wennberg, P. O.: Emission factors for open and domestic biomass burning for use in atmospheric models, Atmos. Chem. Phys., 11(9), 4039–4072, doi:10.5194/acp-11-4039-2011, 2011.

Andreae, M. O.: Emission of trace gases and aerosols from biomass burning - An updated assessment, Atmos. Chem. Phys., 19(13), 8523–8546, doi:10.5194/acp-19-8523-2019, 2019.

Andreae, M. O. and Merlet, P.: Emissions of trace gases and aerosols from biomass burning, Global Biogeochem. Cycles, 15(4), 955–966, doi:10.1029/2000GB001382, 2001.

Baldassarre, G., Pozzoli, L., Schmidt, C. C., Unal, A., Kindap, T., Menzel, W. P., Whitburn, S., Coheur, P. F., Kavgaci, A. and Kaiser, J. W.: Using SEVIRI fire observations to drive smoke plumes in the CMAQ air quality model: the case of Antalya in 2008, Atmos. Chem. Phys., 15, 8539–8558, doi:10.5194/acpd-15-1-2015, 2015.

Bowman, D. M. J. S., Balch, J. K., Artaxo, P., Bond, W. J., Carlson, J. M., Cochrane, M. A., D'Antonio, C. M., DeFries, R. S., Doyle, J. C., Harrison, S. P., Johnston, F. H., Keeley, J. E., Krawchuk, M. A., Kull, C. A., Marston, J. B., Moritz, M. A., Prentice, I. C., Roos, C. I., Scott, A. C., Swetnam, T. W., van der Werf, G. R. and Pyne, S. J.: Fire in the earth system, Science (80-.)., 324(5926), 481–484, doi:10.1126/science.1163886, 2009.

Cheng, Z., Wang, S., Fu, X., Watson, J. G., Jiang, J., Fu, Q., Chen, C., Xu, B., Yu, J., Chow, J. C. and Hao, J.: Impact of biomass burning on haze pollution in the Yangtze River delta, China: A case study in summer 2011, Atmos. Chem. Phys., 14(9), 4573–4585, doi:10.5194/acp-14-4573-2014, 2014.

Chevallier, F., Fortems, A., Bousquet, P., Pison, I., Szopa, S., Devaux, M. and Hauglustaine, D. A.: African CO emissions between years 2000 and 2006 as estimated from MOPITT observations, Biogeosciences, 6(1), 103–111, doi:10.5194/bg-6-103-2009, 2009.

Chin, M., Ginoux, P., Kinne, S., Torres, O., Holben, B., Duncan, B. N., Martin, R. V, Logan, J. A., Higurashi, A. and Nakajima, T.: Tropospheric Aerosol Optical Thickness from the GOCART Model and

Comparisons with Satellite and Sun Photometer Measurements, J. Atmos. Sci., 59(3), 461–483, doi:10.1175/1520-0469(2002)059<0461:TAOTFT>2.0.CO;2, 2002.

Choi, M. W., Lee, J. H., Woo, J. W., Kim, C. H. and Lee, S. H.: Comparison of PM2.5 chemical components over East Asia simulated by the WRF-Chem and WRF/CMAQ models: On the models' prediction inconsistency, Atmosphere (Basel)., 10(10), doi:10.3390/atmos10100618, 2019.

Formenti, P., Elbert, W., Maenhaut, W., Haywood, J. M., Osborne, S. and Andreae, M. O.: Inorganic and carbonaceous aerosols during the Southern African Regional Science Initiative (SAFARI 2000) experiment: Chemical characteristics, physical properties, and emission data or smoke from African biomass burning, J. Geophys. Res. D Atmos., 108(13), 1–16, doi:10.1029/2002jd002408, 2003.

Forster, P., Ramaswamy, V., Artaxo, P., Berntsen, T., Betts, R., Fahey, D. W., Haywood, J. M., Lean, J., Lowe, D. C., Myhre, G., Nganga, J., Prinn, R., Raga, G., Schulz, M. and Van Dorland, R.: Changes in Atmospheric Constituents and in Radiative Forcing (IPCC 2007), Change, 30(22), 129–234, doi:10.1103/PhysRevB.77.220407, 2007.

Freeborn, P. H., Wooster, M. J., Hao, W. M., Ryan, C. A., Nordgren, B. L., Baker, S. P. and Ichoku, C.: Relationships between energy release , fuel mass loss , and trace gas and aerosol emissions during laboratory biomass fires, , 113, 1–17, doi:10.1029/2007JD008679, 2008.

Garcia-menendez, F., Hu, Y. and Odman, M. T.: Science of the Total Environment Simulating smoke transport from wildland fi res with a regional-scale air quality model : Sensitivity to spatiotemporal allocation of fi re emissions, Sci. Total Environ., 493, 544–553, doi:10.1016/j.scitotenv.2014.05.108, 2014.

Giglio, L., Schroeder, W. and Justice, C. O.: The collection 6 MODIS active fire detection algorithm and fire products, Remote Sens. Environ., 178, 31–41, doi:10.1016/j.rse.2016.02.054, 2016.

Hall, J. V., Zhang, R., Schroeder, W., Huang, C. and Giglio, L.: Validation of GOES-16 ABI and MSG SEVIRI active fire products, Int. J. Appl. Earth Obs. Geoinf., 83(August), 101928, doi:10.1016/j.jag.2019.101928, 2019.

Hawbaker, T. J., Vanderhoof, M. K., Beal, Y. J., Takacs, J. D., Schmidt, G. L., Falgout, J. T., Williams, B., Fairaux, N. M., Caldwell, M. K., Picotte, J. J., Howard, S. M., Stitt, S. and Dwyer, J. L.: Mapping burned areas using dense time-series of Landsat data, Remote Sens. Environ., 198(September), 504–522,

doi:10.1016/j.rse.2017.06.027, 2017.

Holben, B., Tanre, D., Smirnov, A., Eck, T. F., Slutsker, I., Abuhassan, N., Newcomb, W. W., Schafer, J. S., Chatenet, B., Lavenu, F., Kaufman, Y., Castle, J. V., Setzer, A., Markham, B., Clark, D., Frouin, R., Halthore, R., Karneli, A. and O'Neill, N. T.: An Emerging Ground- based Aerosol Climatology: Aerosol Optical Depth from AERONET, J. Geophys. Res., 106(Dll), 12067–12097, 2001.

Hu, J., Chen, J., Ying, Q. and Zhang, H.: One-year simulation of ozone and particulate matter in China using WRF/CMAQ modeling system, Atmos. Chem. Phys., 16(16), 10333–10350, doi:10.5194/acp-16-10333-2016, 2016.

Ichoku, C. and Ellison, L.: Global top-down smoke-aerosol emissions estimation using satellite fire radiative power measurements, Atmos. Chem. Phys., 14(13), 6643–6667, doi:10.5194/acp-14-6643-2014, 2014.

Ito, A., Penner, J. E., Prather, M. J., De Campos, C. P., Houghton, R. A., Kato, T., Jain, A. K., Yang, X., Hurtt, G. C., Frolking, S., Fearon, M. G., Chini, L. P., Wang, A. and Price, D. T.: Can we reconcile differences in estimates of carbon fluxes from land-use change and forestry for the 1990s?, Atmos. Chem. Phys., 8(12), 3291–3310, doi:10.5194/acp-8-3291-2008, 2008.

Kaiser, J. W., Heil, A., Andreae, M. O., Benedetti, A., Chubarova, N., Jones, L., Morcrette, J. J., Razinger, M., Schultz, M. G., Suttie, M. and van der Werf, G. R.: Biomass burning emissions estimated with a global fire assimilation system based on observed fire radiative power, Biogeosciences, 9(1), 527–554, doi:10.5194/bg-9-527-2012, 2012.

Keywood, M., Kanakidou, M., Stohl, A., Dentener, F., Grassi, G., Meyer, C. P., Torseth, K., Edwards, D., Thompson, A. M., Lohmann, U. and Burrows, J.: Fire in the air: Biomass burning impacts in a changing climate, Crit. Rev. Environ. Sci. Technol., 43(1), 40–83, doi:10.1080/10643389.2011.604248, 2013.

Kopacz, M., Jacob, D. J., Fisher, J. A., Logan, J. A., Zhang, L., Megretskaia, I. A., Yantosca, R. M., Singh, K., Henze, D. K., Burrows, J. P., Buchwitz, M., Khlystova, I., McMillan, W. W., Gille, J. C., Edwards, D. P., Eldering, A., Thouret, V. and Nedelec, P.: Global estimates of CO sources with high resolution by adjoint inversion of multiple satellite datasets (MOPITT, AIRS, SCIAMACHY, TES), Atmos. Chem. Phys., 10(3), 855–876, doi:10.5194/acp-10-855-2010, 2010.

https://doi.org/10.5194/acp-2022-193
Preprint. Discussion started: 25 April 2022

Koplitz, S. N., Nolte, C. G., Pouliot, G., Vukovich, J. M. and Beidler, J.: Influence of uncertainties in burned area estimates on modeled wildland fire PM2.5 and ozone pollution in the contiguous U.S., Atmos. Environ., 191, 328–339, doi:10.1016/j.atmosenv.2018.08.020, 2018.

Kuik, F., Lauer, A., Beukes, J. P., Van Zyl, P. G., Josipovic, M., Vakkari, V., Laakso, L. and Feig, G. T.: The anthropogenic contribution to atmospheric black carbon concentrations in southern Africa: A WRF-Chem modeling study, Atmos. Chem. Phys., 15(15), 8809–8830, doi:10.5194/acp-15-8809-2015, 2015.

Kukkonen, J., Olsson, T., Schultz, D. M., Baklanov, A., Klein, T., Miranda, A. I., Monteiro, A., Hirtl, M., Tarvainen, V., Boy, M., Peuch, V. H., Poupkou, A., Kioutsioukis, I., Finardi, S., Sofiev, M., Sokhi, R., Lehtinen, K. E. J., Karatzas, K., San José, R., Astitha, M., Kallos, G., Schaap, M., Reimer, E., Jakobs, H. and Eben, K.: A review of operational, regional-scale, chemical weather forecasting models in Europe, Atmos. Chem. Phys., 12(1), 1–87, doi:10.5194/acp-12-1-2012, 2012.

Landgraf, J., Aan de Brugh, J., Scheepmaker, R. A., Borsdorff, T., Hu, H., Houweling, S., Butz, A., Aben, I. and Hasekamp, O.: Carbon monoxide total column retrievals from TROPOMI shortwave infrared measurements, Atmos. Meas. Tech., 9(10), 4955–4975, doi:10.5194/amt-9-4955-2016, 2016.

Langmann, B., Duncan, B., Textor, C., Trentmann, J. and van der Werf, G. R.: Vegetation fire emissions and their impact on air pollution and climate, Atmos. Environ., 43(1), 107–116, doi:10.1016/j.atmosenv.2008.09.047, 2009.

Lavorel, S., Flannigan, M. D., Lambin, E. F. and Scholes, M. C.: Vulnerability of land systems to fire: Interactions among humans, climate, the atmosphere, and ecosystems, Mitig. Adapt. Strateg. Glob. Chang., 12(1), 33–53, doi:10.1007/s11027-006-9046-5, 2007.

Van Leeuwen, T. T., van der Werf, G. R., Hoffmann, A. A., Detmers, R. G., Rücker, G., French, N. H. F., Archibald, S., Carvalho, J. A., Cook, G. D., de Groot, W. J., Hély, C., Kasischke, E. S., Kloster, S., McCarty, J. L., Pettinari, M. L., Savadogo, P., Alvarado, E. C., Boschetti, L., Manuri, S., Meyer, C. P., Siegert, F., Trollope, L. A. and Trollope, W. S. W.: Biomass burning fuel consumption rates: a field measurement database, Biogeosciences Discuss., 11(6), 8115–8180, doi:10.5194/bgd-11-8115-2014, 2014.

Lyapustin, A., Wang, Y., Korkin, S. and Huang, D.: MODIS Collection 6 MAIAC algorithm, Atmos. Meas. Tech., 11(10), 5741–5765, doi:10.5194/amt-11-5741-2018, 2018.

https://doi.org/10.5194/acp-2022-193
Preprint. Discussion started: 25 April 2022


Atmospheric Chemistry and Physics Discussions

Mota, B. and Wooster, M. J.: A new top-down approach for directly estimating biomass burning emissions and fuel consumption rates and totals from geostationary satellite fi re radiative power (FRP), Remote Sens. Environ., 206(February 2017), 45–62, doi:10.1016/j.rse.2017.12.016, 2018.

Nguyen, H. M. and Wooster, M. J.: Advances in the estimation of high Spatio-temporal resolution pan-African top-down biomass burning emissions made using geostationary fire radiative power (FRP) and MAIAC aerosol optical depth (AOD) data, Remote Sens. Environ., 248(November 2019), 111971, doi:10.1016/j.rse.2020.111971, 2020.

Pechony, O., Shindell, D. T. and Faluvegi, G.: Direct top-down estimates of biomass burning CO emissions using TES and MOPITT versus bottom-up GFED inventory, J. Geophys. Res. Atmos., 118(14), 8054–8066, doi:10.1002/jgrd.50624, 2013.

Quennehen, B., Schwarzenboeck, A., Matsuki, A., Burkhart, J. F., Stohl, A., Ancellet, G. and Law, K. S.: Anthropogenic and forest fire pollution aerosol transported to the Arctic: Observations from the POLARCAT-France spring campaign, Atmos. Chem. Phys., 12(14), 6437–6454, doi:10.5194/acp-12-6437-2012, 2012.

Randerson, J. T., Chen, Y., van der Werf, G. R., Rogers, B. M. and Morton, D. C.: Global burned area and biomass burning emissions from small fires, J. Geophys. Res. G Biogeosciences, 117(4), doi:10.1029/2012JG002128, 2012.

Reddington, C. L., Spracklen, D. V., Artaxo, P., Ridley, D. A., Rizzo, L. V. and Arana, A.: Analysis of particulate emissions from tropical biomass burning using a global aerosol model and long-term surface observations, Atmos. Chem. Phys., 16(17), 11083–11106, doi:10.5194/acp-16-11083-2016, 2016.

Reid, J. S., Eck, T. F., Christopher, S. A., Koppmann, R., Dubovik, O., Eleuterio, D. P., Holben, B., Reid, E. A. and Zhang, J.: A review of biomass burning emissions part III: Intensive optical properties of biomass burning particles, Atmos. Chem. Phys., 5(3), 827–849, doi:10.5194/acp-5-827-2005, 2005.

Reid, J. S., Hyer, E. J., Prins, E., Westphal, D. L., Zhang, J., Wang, J., Christopher, S. A., Curtis, C. A., Schmidt, C. C., Eleuterio, D. P., Richardson, K. A. and Hoffman, J.: Global monitoring and forecasting of biomass-burning smoke: Description of and lessons from the fire Locating and Modeling of Burning Emissions (FLAMBE) program, IEEE J. Sel. Top. Appl. Earth Obs. Remote Sens., 2(3), 144–162, doi:10.1109/JSTARS.2009.2027443, 2009.

Roberts, G., Wooster, M. J., Perry, G. L. W., Drake, N., Rebelo, L. M. and Dipotso, F.: Retrieval of biomass combustion rates and totals from fire radiative power observations: Application to southern Africa using geostationary SEVIRI imagery, J. Geophys. Res. Atmos., 110(21), 1–19, doi:10.1029/2005JD006018, 2005.

Roberts, G., Wooster, M. J., Xu, W., Freeborn, P. H., Morcrette, J. J., Jones, L., Benedetti, A., He, J., Fisher, D. and Kaiser, J. W.: LSA SAF Meteosat FRP products-Part 2: Evaluation and demonstration for use in the Copernicus Atmosphere Monitoring Service (CAMS), Atmos. Chem. Phys., 15(22), 13241–13267, doi:10.5194/acp-15-13241-2015, 2015.

Roteta, E., Bastarrika, A., Padilla, M., Storm, T. and Chuvieco, E.: Development of a Sentinel-2 burned area algorithm: Generation of a small fire database for sub-Saharan Africa, Remote Sens. Environ., 222(March), 1–17, doi:10.1016/j.rse.2018.12.011, 2019.

Seiler, W. and Crutzen, P. J.: Estimates of gross and net fluxes of carbon between the biosphere and the atmosphere from biomass burning, Clim. Change, 2(3), 207–247, doi:10.1007/BF00137988, 1980.

Syrakov, D., Prodanova, M., Georgieva, E., Etropolska, I. and Slavov, K.: Simulation of European air quality by WRF-CMAQ models using AQMEII-2 infrastructure, J. Comput. Appl. Math., 293, 232–245, doi:10.1016/j.cam.2015.01.032, 2016.

Tsela, P. L., Van Helden, P., Frost, P., Wessels, K. and Archibald, S.: Validation of the modis burned-area products across different biomes in South Africa, Int. Geosci. Remote Sens. Symp., (May 2016), 3652–3655, doi:10.1109/IGARSS.2010.5650253, 2010.

Vermote, E., Ellicott, E., Dubovik, O., Lapyonok, T., Chin, M., Giglio, L. and Roberts, G.: An approach to estimate global biomass burning emissions of organic and black carbon from MODIS fire radiative power, J. Geophys. Res. Atmos., 114(18), 1–22, doi:10.1029/2008JD011188, 2009.

Vongruang, P., Wongwises, P. and Pimonsree, S.: Assessment of fire emission inventories for simulating particulate matter in Upper Southeast Asia using WRF-CMAQ, Atmos. Pollut. Res., 8(5), 921–929, doi:10.1016/j.apr.2017.03.004, 2017.

van der Werf, G. R., Randerson, J. T., Giglio, L., Collatz, G. J., Kasibhatla, P. S. and Arellano, A. F., J.: Interannual variability in global biomass burning emissions from 1997 to 2004, Atmos. Chem. Phys., 6(11), 3423–3441, doi:10.5194/acpd-6-3175-2006, 2006.

https://doi.org/10.5194/acp-2022-193
Preprint. Discussion started: 25 April 2022

van der Werf, G. R., Randerson, J. T., Giglio, L., Collatz, G. J., Mu, M., Kasibhatla, P. S., Morton, D. C., Defries, R. S., Jin, Y. and Van Leeuwen, T. T.: Global fire emissions and the contribution of deforestation, savanna, forest, agricultural, and peat fires (1997-2009), Atmos. Chem. Phys., 10(23), 11707–11735, doi:10.5194/acp-10-11707-2010, 2010.

van der Werf, G. R., Randerson, J. T., Giglio, L., Van Leeuwen, T. T., Chen, Y., Rogers, B. M., Mu, M., van Marle, M. J. E., Morton, D. C., Collatz, G. J., Yokelson, R. J. and Kasibhatla, P. S.: Global fire emissions estimates during 1997-2016, Earth Syst. Sci. Data Discuss., 1–43, doi:10.5194/essd-2016-62, 2017.

Wiedinmyer, C., Akagi, S. K., Yokelson, R. J., Emmons, L. K., Al-Saadi, J. A., Orlando, J. J. and Soja, A. J.: The Fire INventory from NCAR (FINN): A high resolution global model to estimate the emissions from open burning, Geosci. Model Dev., 4(3), 625–641, doi:10.5194/gmd-4-625-2011, 2011.

Wooster, M. J., Freeborn, P. H., Archibald, S., Oppenheimer, C., Roberts, G., Smith, T. E. L., Govender, N., Burton, M. and Palumbo, I.: Field determination of biomass burning emission ratios and factors via open-path FTIR spectroscopy and fire radiative power assessment: Headfire, backfire and residual smouldering combustion in African savannahs, Atmos. Chem. Phys., 11(22), 11591–11615, doi:10.5194/acp-11-11591-2011, 2011.

Wooster, M. J., Roberts, G., Freeborn, P. H., Xu, W., Govaerts, Y., Beeby, R., He, J., Lattanzio, A., Fisher, D. and Mullen, R.: LSA SAF Meteosat FRP products-Part 1: Algorithms, product contents, and analysis, Atmos. Chem. Phys., 15(22), 13217–13239, doi:10.5194/acp-15-13217-2015, 2015.

Worden, H. M., Deeter, M. N., Edwards, D. P., Gille, J. C., Drummond, J. R. and Nédélec, P.: Observations of near-surface carbon monoxide from space using MOPITT multispectral retrievals, J. Geophys. Res. Atmos., 115(18), 1–12, doi:10.1029/2010JD014242, 2010.

Xu, W., Wooster, M. J., Roberts, G. and Freeborn, P. H.: New GOES imager algorithms for cloud and active fi re detection and fi re radiative power assessment across North , South and Central America, Remote Sens. Environ., 114(9), 1876–1895, doi:10.1016/j.rse.2010.03.012, 2010.

Xu, W., Wooster, M. J., Kaneko, T., He, J., Zhang, T. and Fisher, D.: Major advances in geostationary fire radiative power (FRP) retrieval over Asia and Australia stemming from use of Himarawi-8 AHI, Remote Sens. Environ., 193, 138–149, doi:10.1016/j.rse.2017.02.024, 2017.

https://doi.org/10.5194/acp-2022-193
Preprint. Discussion started: 25 April 2022


Atmospheric Chemistry and Physics Discussions

Yang, Z., Wang, J., Ichoku, C., Hyer, E. J. and Zeng, J.: Mesoscale modeling and satellite observation of transport and mixing of smoke and dust particles over northern sub-Saharan African region, J. Geophys. Res. Atmos., 118(21), 12139–12157, doi:10.1002/2013JD020644, 2013.

Yu, S., Eder, B., Dennis, R., Chu, S.-H. and Schwartz, S. E.: New unbiased symmetric metrics for evaluation of air quality models, Atmos. Sci. Lett., 7(1), 26–34, doi:10.1002/asl.125, 2006.

Zhang, F., Wang, J., Ichoku, C., Hyer, E. J., Yang, Z., Ge, C., Su, S., Zhang, X., Kondragunta, S., Kaiser, J. W., Wiedinmyer, C. and Da Silva, A.: Sensitivity of mesoscale modeling of smoke direct radiative effect to the emission inventory: A case study in northern sub-Saharan African region, Environ. Res. Lett., 9(7), doi:10.1088/1748-9326/9/7/075002, 2014.

Zhang, X., Kondragunta, S., Schmidt, C. and Kogan, F.: Near real time monitoring of biomass burning particulate emissions (PM2.5) across contiguous United States using multiple satellite instruments, Atmos. Environ., 42(29), 6959–6972, doi:10.1016/j.atmosenv.2008.04.060, 2008.

Zheng, B., Chevallier, F., Ciais, P., Yin, Y. and Wang, Y.: On the Role of the Flaming to Smoldering Transition in the Seasonal Cycle of African Fire Emissions, Geophys. Res. Lett., 45(21), 11,998-12,007, doi:10.1029/2018GL079092, 2018.